Xist upstream deletion leads to dysregulation of *Xist* and autosomal gene expression

Sudeshna Majumdar, Lakshmi Sowjanya Bammidi, Hemant C. Naik, et al.

Genome Res. 2025 35: 1992-2010 originally published online August 6, 2025
Access the most recent version at doi:10.1101/gr.279822.124

Research

Xist upstream deletion leads to dysregulation of *Xist* and autosomal gene expression

Sudeshna Majumdar,[1,4] Lakshmi Sowjanya Bammidi,[1,5] Hemant C. Naik,[1,2] Avinchal Manhas,[1] Runumi Baro,[1] Akash Kalita,[1,6] Amlan Jyoti Naskar,[1] Sundarraj Nidharshan,[3] Girija S. Bariha,[1,7] Dimple Notani,[3] and Srimonta Gayen[1]

[1]*Department of Developmental Biology and Genetics, Indian Institute of Science, Bangalore-560012, India;* [2]*Functional Genomics and Bioinformatics Unit, The University of Trans-Disciplinary Health Sciences and Technology (TDU), Bangalore 560064, India;* [3]*National Centre for Biological Sciences, Tata Institute of Fundamental Research, Bangalore 560065, India*

Xist long noncoding RNA is the master regulator of the X-Chromosome inactivation (XCI) process. *Xist* is expressed from the inactive X and coats the inactive X to facilitate XCI. *Cis*-regulation of *Xist* expression remains poorly understood in the context of maintenance of XCI. Here, we have explored the role of the *Xist* upstream sequences (~6 kb) lying between *Tsix* and *Jpx* in the regulation of *Xist* and XCI in mouse extra-embryonic endoderm stem cells (XEN), which represent the maintenance phase of imprinted XCI. Here, we show that the deletion of this *Xist* upstream sequence in the inactive X leads to the upregulation of *Xist* expression accompanied by the dispersal of the *Xist* cloud. Notably, we find the loss of enrichment of repressive marks such as H3K27me3, H4K20mel, and MacroH2A, except that of H2AKll9ub, in dispersed *Xist* nuclei. However, X-linked genes remain silent despite *Xist* dispersal and loss of enrichment of repressive marks. Notably, we find that many autosomal genes, including cohesin *Rad21*, are dysregulated in *Xist*-upstream-deleted cells. Additionally, we demonstrate that *Xist*-upstream deletion leads to alterations of topological contacts of the *Xist* locus with its upstream positive regulator *Ftx* and across the inactive X and autosomes. Finally, we show genome-wide alterations of the occupancy of architectural proteins CTCF/RAD2l, including at many loci of the inactive X such as the *Xist* upstream regions and the *Firre* locus, which is critical for maintaining inactive X conformation. Taken together, we demonstrate that the *Xist* upstream sequence imparts a multifaceted role in genome regulation beyond the XCI.

[Supplemental material is available for this article.]

X-Chromosome inactivation (XCI) is a process by which female mammals compensate for the dosage of X-linked gene expression between sexes (Lyon 1961; Gayen et al. 2015, 2016). XCI is an excellent model system for understanding regulatory elements involved in epigenetic regulation. In mouse, there are two forms of XCI: imprinted and random (Takagi and Sasaki 1975; Okamoto et al. 2004; Sarkar et al. 2015; Maclary et al. 2017; Harris et al. 2019; Mandal et al. 2020). At the onset of early embryonic development (~four-cell stage), all cells undergo imprinted XCI, where the paternal X is inactivated and later switches to random XCI in embryonic epiblast cells, where either paternal or maternal X is chosen for the inactivation (Mak et al. 2004; Maclary et al. 2014; Naik et al. 2022; Samanta et al. 2022). Both imprinted and random XCI is orchestrated by *Xist* long noncoding RNA (lncRNA). *Xist* is expressed from the inactive X and coats the inactive X. *Xist* recruits different chromatin modifiers to enable heterochromatinization of the inactive X (Maclary et al. 2014; Żylicz and Heard 2020; Boeren and Gribnau 2021). Expression of *Xist* is regulated through a series of regulatory elements encoded from the X inactivation center (*Xic*), a region (~800 kb) encompassing *Xist*. Xic is organized into two topologically associated domains (TADs)—(1) the *Tsix*-TAD, comprised of negative regulators of *Xist* like *Tsix*, *Xite*, and *Linx*; and (2) the *Xist*-TAD consisting of *Xist* and its positive regulators *Jpx*, *Ftx*, *Xert*, *Rlim* (Lee et al. 1999; Ogawa and Lee 2003; Jonkers et al. 2009; Tian et al. 2010; Chureau et al. 2011; Nora et al. 2012; van Bemmel et al. 2019; Galupa et al. 2020, 2022). In recent years, the role and mechanisms of different *Xic*-encoded *Xist* activators (*Jpx*, *Ftx*, *Rlim, Xert)* located upstream of the *Xist* locus have been extensively studied in the context of random XCI (Shin et al. 2014; Furlan et al. 2018; Collombet et al. 2020; Gjaltema et al. 2022; Rosspopoff et al. 2023). However, *Xist* activation mechanisms in imprinted XCI remain underexplored. Although few studies explored the role of *Ftx*, *Rlim*, and enhancer elements of the *Xert* locus in the induction of *Xist* expression during the initiation of imprinted XCI (Shin et al. 2010; Soma et al. 2014; Ravid Lustig et al. 2023), regulatory elements involved in the *Xist* expression during the maintenance phase of imprinted XCI remain largely unclear. Here, we have explored the role of the *Xist* upstream sequences (~6 kb) lying between *Tsix* and *Jpx* in regulation of *Xist* and XCI in mouse extraembryonic endoderm stem cells (XEN), which represent a

Present addresses: [4]Cell Biology of Genomes, National Cancer Institute, National Institutes of Health, Bethesda, MD 20892, USA; [5]Department of Nephrology, Division of Medical Sciences, Tata-IISc Medical School, Indian Institute of Science, Bangalore 560012, India; [6]Department of Developmental Genetics, Max Planck Institute for Heart and Lung Research, Bad Nauheim 61231, Germany; [7]Cell and Molecular Biology laboratory, Centre for Incubation, Innovation, Research and Consultancy (CIIRC), Jyothy Institute of Technology, Bengaluru 560082, India
Corresponding author: srimonta@iisc.ac.in
Article published online before print. Article, supplemental material, and publication date are at https://www.genome.org/cgi/doi/10.1101/gr.279822.124.

35:1992–2010 Published by Cold Spring Harbor Laboratory Press; ISSN 1088-9051/25; www.genome.org

maintenance phase of imprinted XCI ex vivo. We show that deletion of this *Xist* upstream sequence in the inactive X has diverse effects, such as upregulation of *Xist* expression, dispersal of *Xist* clouds, alteration of topological interactions of the *Xist* locus, and dysregulation of autosomal gene expression.

Results

Xist and its upstream regulators in XEN cells with imprinted inactive X exhibit topological interactions similar to random inactivated X but have different chromatin features

It has been demonstrated that the proper topological organization and chromatin features of the *Xic* are important for the proper regulation of *Xist* expression and the orchestration of XCI. The *Xic* comprises two TADs: the *Xist* TAD and the *Tsix* TAD (Nora et al. 2012; van Bemmel et al. 2019). The *Tsix*-TAD comprises the negative regulators of *Xist*, like *Tsix*, *Xite*, and the *Xist*-TAD consists of *Xist* and its positive regulators *Jpx*, *Ftx*, and *Rlim* (Fig. 1A). Upon XCI, TADs disappear broadly across the inactive X except for a few transcribing loci (Nora et al. 2012; Minajigi et al. 2015; Giorgetti et al. 2016). At the *Xic*, upon XCI, the *Tsix*-TAD disappears; however, *Xist*-TAD–like interactions persist (Nora et al. 2012; Giorgetti et al. 2016). In recent years, *cis*-regulatory mechanisms of *Xist* activators located upstream of *Xist* (*Jpx*, *Ftx*, *Rlim)* have been studied in the context of random XCI (Furlan et al. 2018; Rosspopoff et al. 2023; Malcore and Kalantry 2024). Here, we investigated whether similar *Xist*-TAD–like interactions exist in XEN cells, which represent the maintenance phase of imprinted XCI. To explore this, we profiled the topological interactions of the *Xist* locus by performing allele-specific circular chromosome conformation capture sequencing (4C-seq) in XEN cells. The XEN cell used for this study is a hybrid cell line derived from two divergent mouse strains *Mus musculus* (Mus) and *Mus molossinus* (Mol), which allowed us to perform allele-specific analysis (Fig. 1B; Arava et al. 2023; Naik et al. 2024). Moreover, paternal X is inactivated in XEN cells, which helped us to distinguish between active X- and inactive X-specific signals (Arava et al. 2023; Naik et al. 2024). From a viewpoint near the *Xist* transcriptional start sites, we found major contacts of the *Xist* with the regions encompassing *Ftx* loci on the inactive X in XEN cells (Fig. 1C). These interactions were found to be less in the active X Chromosome; however, we observed that *Xist* interacts at the 3′ region of the *Slc16a2* locus of the active X (Fig. 1C). Additionally, we observed contacts of the *Xist* locus with a few loci within the adjacent *Tsix*-TAD, suggesting the existence of inter-TAD interactions (Fig. 1C). Next, we compared the *Xist* locus interactions of XEN cells with the mouse embryonic fibroblast cells (MEF), which represent the random form of XCI. We performed virtual 4C analysis using the available Hi-C data of MEF cells (Du et al. 2024). This MEF cell line is a hybrid (PWK/Phj X C57BL/6N) and derived from a single clone having PWK-X as the inactive X, which allowed us to distinguish between active versus inactive X in our analysis. We observed that the major contacts of the *Xist* in MEF cells belong to the regions encompassing *Ftx* loci on the inactive X, like XEN cells (Fig. 1D; Supplemental Fig. S1A). Next, we profiled the enrichment of CTCF and cohesin (RAD21) in XEN cells across the *Xic* in the active X Chromosome versus inactive X Chromosome through allele-specific chromatin immunoprecipitation sequencing (ChIP-seq) analysis. We also analyzed an available CUT&RUN data set of CTCF and another subunit of the cohesin complex SMC3 for XEN cells (Supplemental Table S1; Du et al. 2024). We observed that the allelic CTCF enrichment profile was well aligned between the ChIP-seq and CUT&RUN data sets (Supplemental Fig. S1B). Similarly, the enrichment of RAD21 (ChIP-seq) with the SMC3 (CUT&RUN) looked similar but differed to some extent (Supplemental Fig. S1C). We found that the *Xist* and *Ftx* loci were flanked by convergent arrays of CTCF binding sites, and these CTCF binding sites were often co-enriched with cohesins (SMC3 and RAD21), suggesting cohesin and CTCF-mediated looping between these loci as observed in our 4C analysis (Fig. 1E). Next, we compared the CTCF and SMC3 enrichment of XEN cells with the available data set of MEF cells with random XCI (Supplemental Table S1; Du et al. 2024). We found that the *Xist* and *Ftx* locus in MEF cells also flanked by CTCF and cohesins, like XEN cells (Supplemental Fig. S1D). Next, we profiled the enrichment of H3K27ac and H3K4me1 in the *Xist* upstream regulatory region of XEN cells through ChIP-seq. We also analyzed the available data set for H3K27ac in XEN cells (Supplemental Table S1; Du et al. 2024). We observed a strong enrichment of H3K27ac and H3K4me1 at the *Xist* upstream region encompassing *Xist* and *Ftx* on the inactive X, indicating an enhancer-like property of this region (Fig. 1F). Similar enrichment was observed on the active X as well (Fig. 1F). Notably, we found that such enrichment of H3K27ac was absent in MEF cells with random XCI (Fig. 1F). However, there were few major peaks observed near the *Xist* and *Ftx* loci (Fig. 1F). Additionally, we analyzed the available H3K4me1 data set from trophoblast stem cells (TSC) with imprinted XCI (Calabrese et al. 2012). We found similar enrichment of H3K4me1 across the *Xist* and *Ftx* loci in TSCs (Fig. 1F). Taken together, we conclude that, in both XEN (imprinted) and MEF (random) cells, the major contacts of the *Xist* locus on the inactive X belong to the regions encompassing *Ftx* loci; however, the chromatin features of this region are different between them.

Deletion of *Xist* upstream sequence leads to upregulation of *Xist* expression and dispersal of *Xist* clouds

The *cis*-regulation of *Xist* by *Xist* upstream sequences in the context of the maintenance phase of imprinted XCI remains underexplored. Here, we explored the role of the *Xist* upstream sequences (~6 kb) lying between *Tsix* and *Jpx* in the regulation of *Xist* and XCI in XEN cells. We performed an allele-specific analysis of H3K27me3 and H3K9me3 ChIP-seq data to identify the enrichment of these repressive marks at this locus. As expected, we observed very high enrichment of H3K27me3 on the inactive X compared to the active X, whereas enrichment at autosomal alleles was equivalent, thus validating our allelic analysis pipeline (Supplemental Fig. S1E). We find that the *Xist* upstream sequences (~6 kb) lying between *Tsix* and *Jpx* on the inactive X are devoid of enrichment of repressive H3K27me3 (Fig. 2A). However, some enrichment of H3K9me3 appears to be there, although peaks were not called significant with a *Q*-value cutoff <0.05 (Fig. 2A). Moreover, it was previously reported that this region harbors DNase hypersensitive sites (DHSs) in mouse somatic tissues and embryonic stem cells (Fig. 2A; Sheardown et al. 1997; Newall et al. 2001). Additionally, this region has been referred to as being conducive to retrotransposition and harbors two ribosomal protein pseudogenes (*pS19X* and *pS12X*) (Fig. 2A; Rougeulle and Avner 1996; Romer and Ashworth 2000). Notably, this region is enriched with long interspersed elements (LINEs) and short interspersed elements (SINEs), which are believed to play a role in *Xist* spreading, coating, and X-linked gene silencing (Fig. 2A; Lyon 1998; Chaumeil et al. 2006; Chow et al. 2010; Loda et al. 2017).

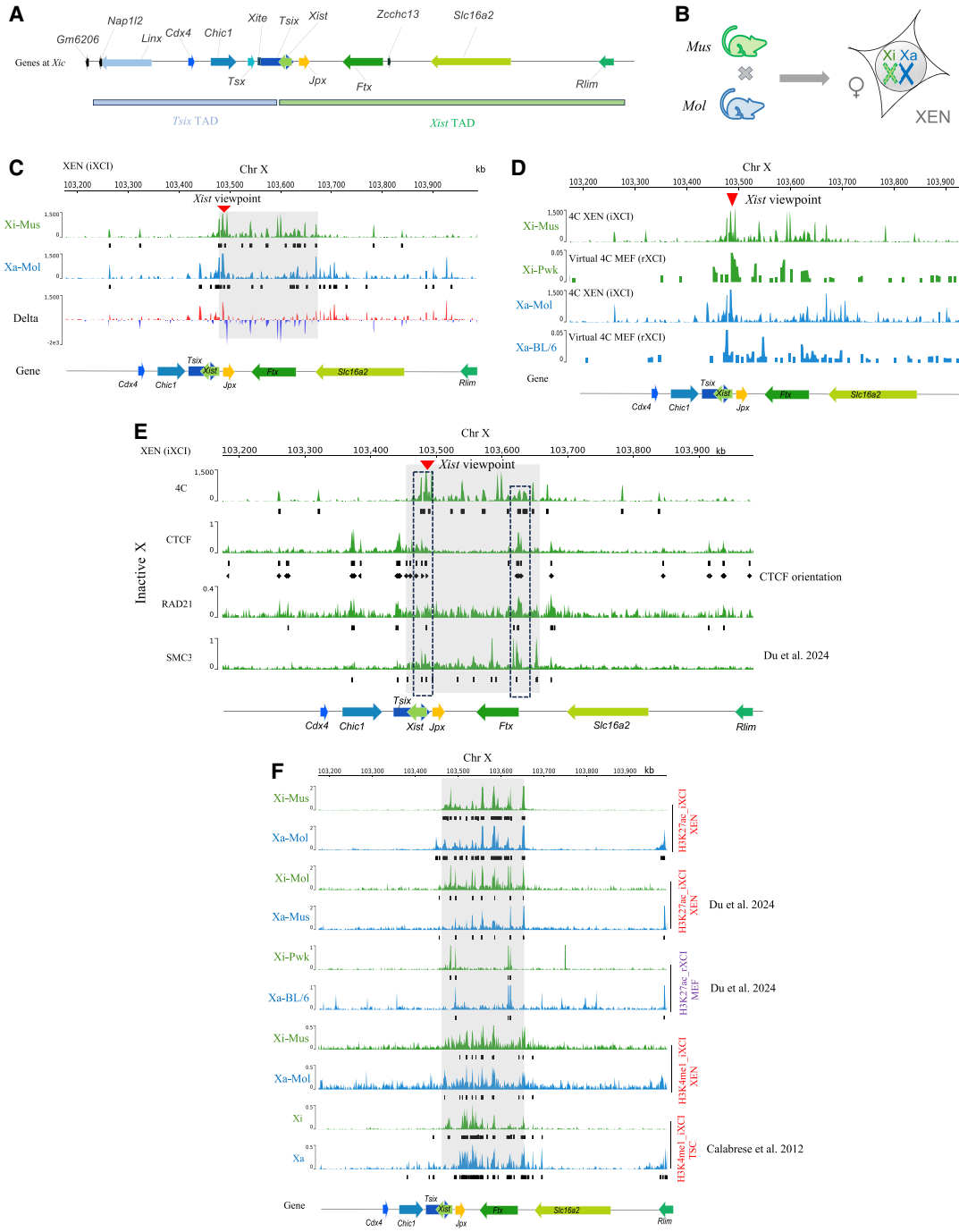

Figure 1. Comparison of *Xist* locus interactions and chromatin features at the *Xic* between imprinted and random X inactivation. (*A*) Schematic representing the linear arrangement of genes across the *Xist* and *Tsix* TADs. (*B*) Diagrammatic representation of hybrid XEN cells derived from a cross between *Mus musculus* (Mus) and *Mus molossinus* (Mol) mice. The X Chromosome derived from *Mus* is the inactive X. (*C*) Allele-specific 4C interaction profile considering *Xist* locus as the viewpoint (marked by red arrow) across the X-inactivation center (*Xic*) in XEN cells (imprinted). Green and blue tracks represent Xi and Xa interaction profiles, respectively. Black boxes *below* each track denote significant interactions (*Q*-value <0.01). Delta plots represent the differences in interactions between Xa versus Xi (red peaks–gain of interactions, and blue peaks–loss of interactions in the Xa compared to the Xi). The shaded area highlights differences in interactions between Xi versus Xa in the region encompassing the *Xist* and *Ftx* loci. (*D*) Plots representing interactions profile of the *Xist* locus across the *Xic* in Xi (green) and Xa (blue) in XEN cells (4C) versus MEFs (Virtual-4C). The red arrow marks the viewpoint. For virtual 4C analysis, Hi-C data for MEF was used from Du et al. (2024). (*E*) Plots showing Xi-specific 4C interaction profile considering *Xist* locus as the viewpoint (marked by red arrow) across the *Xic* and Xi-specific enrichment of CTCF, RAD21, SMC3 in XEN cells. Black boxes *under* each track denote significant peaks. 4C contacts overlapping with CTCF and RAD21/SMC3 peaks are highlighted through dotted boxes. (*F*) Plots showing the ChIP-seq enrichment of H3K27ac in XEN (iXCI) versus MEFs (rXCI) and H3K4me1 in XEN (iXCI) and TSCs (iXCI) in inactive- X (green) and active- X (blue) of the *Xic*. Black boxes denote significant peaks *under* each track. ChIP-seq data set for H3K27ac XEN (Xi^{Mol} Xa^{Mus}) and H3K27ac MEF were obtained from Du et al. (2024) and H3K4me1 TSC was obtained from Calabrese et al. (2012). The shaded area highlights the enrichment pattern of H3K27ac and H3K4me1. iXCI: imprinted X-Chromosome inactivation; rXCI: random X-Chromosome inactivation.

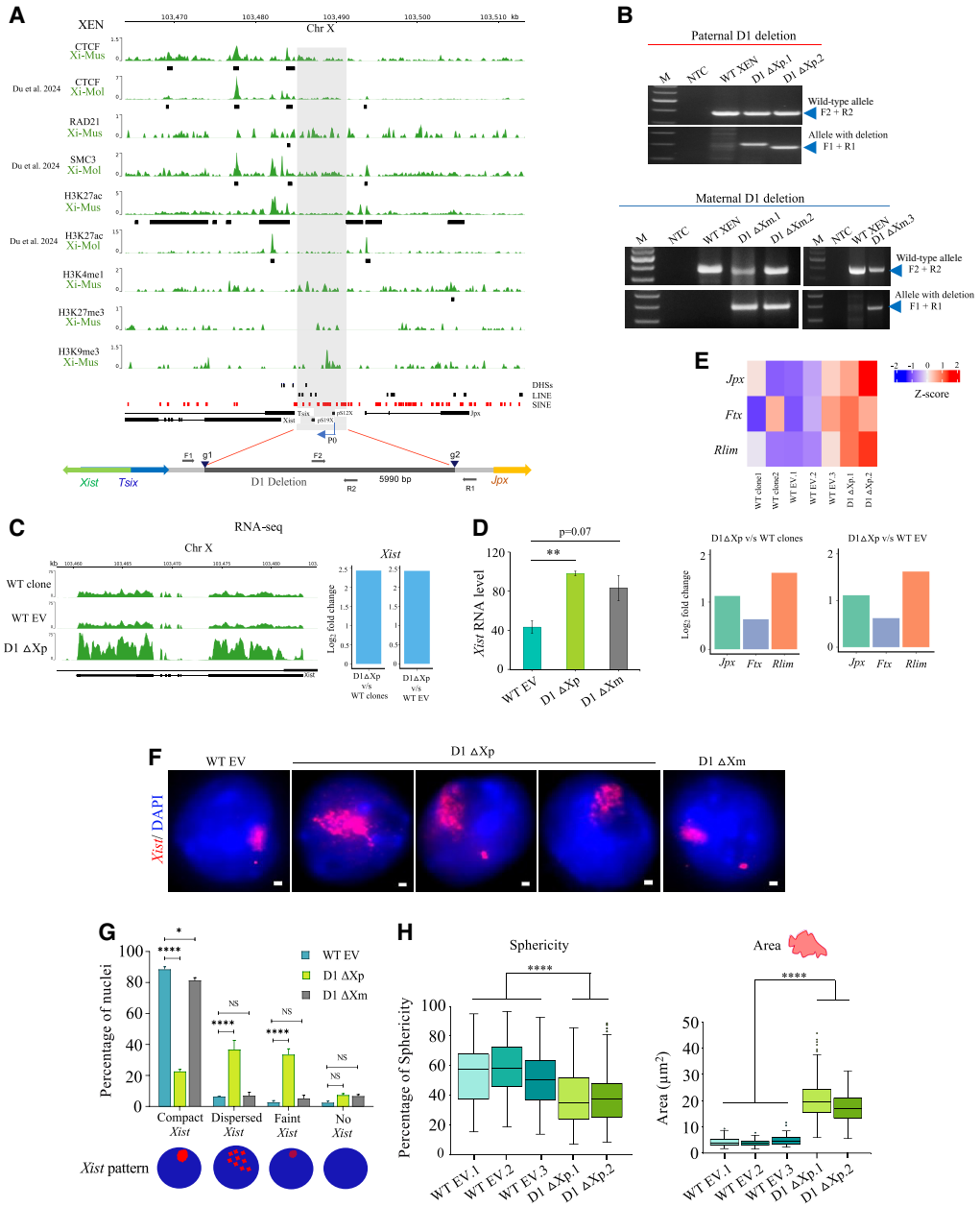

Figure 2. *Xist* upstream deletion leads to *Xist* upregulation and *Xist* dispersal. (*A*) *Top*: Plots showing the enrichment of CTCF, RAD21, SMC3, H3K27ac, H3K4me1, H3K27me3, and H3K9me3 at the *Xist* upstream region targeted for the deletion (shaded) in the Xi of XEN cells. Black boxes denote significant peaks under each track. Enrichment of LINE (black boxes) and SINE (red boxes) elements, DHSs (black boxes) are indicated. Analysis of CTCF XEN (Xi^{Mus} Xa^{Mol}), RAD21, H3K27ac, H3K4me1, H3K27me3, and H3K9me3 is based on ChIP-seq. CUT&RUN data of CTCF XEN (Xi^{Mol} Xa^{Mus}) and SMC3 XEN obtained from Du et al. (2024). *Bottom*: Schematic showing the region intermediate to *Tsix* and *Jpx* that is targeted for deletion in XEN cells. sgRNA binding sites: g1 and g2. PCR primers F2 and R2, and F1 and R1 shown as gray arrows used for amplification of the wild-type allele and the allele with deletion, respectively. (*B*) PCR-based identification of clones having the deletion of the *Xist* upstream region (D1) on the paternal allele (*top*) and maternal allele (*bottom*). Arrowheads represent the position of the expected amplicon. Primer pairs used for each deletion are shown on the *right*. NTC stands for no template control and M for Marker. (*C*) *Left*: Genome browser view of *Xist* expression for WT clones, WT EV, and D1 ΔXp clones as observed through RNA-seq. *Right*: Bar plots representing the $\log_2$ fold change for *Xist* (>2.4 $\log_2$ fold change; FDR ≤0.01) in D1 ΔXp over WT clone and WT EV clones as seen through RNA-seq analysis. (*D*) Analysis of *Xist* expression levels by RT-qPCR in WT EV and D1 deleted clones. *Tbp* is used as the normalizing control. n = 3 biological replicates for each of WT EV and D1 ΔXm and n = 2 for D1 ΔXp was used. Error bars represent the standard error of mean. *P* values (two-tailed t–test): (**) $P \leq 0.01$. (*E*) *Top*: Heat map showing the increased expression of *Jpx*, *Ftx*, and *Rlim* in D1 ΔXp cells compared to the WT clone and WT EV clones. *Bottom*: Plots showing the $\log_2$ fold change in expression levels of *Jpx*, *Ftx*, *Rlim* in D1 ΔXp versus WT clone and WT EV clones as quantified through RNA-seq. (*F*) RNA-FISH using double-stranded DNA probe for *Xist*/*Tsix*-Cy3 (red) in wild-type empty-vector transfected (WT EV) and heterozygous clones of both paternally (D1 ΔXp) and maternally (D1 ΔXm) deleted clones. DAPI (blue) counterstains the nucleus. Scale bars: 1 μm. (*G*) Plot representing the quantification of the *Xist* RNA-FISH signals in WT EV and heterozygous (D1 ΔXp and D1 ΔXm) clones. *Bottom*: Schematic representing different types of *Xist* pattern. n = 3 biological replicates in each of WT EV and D1 ΔXm and n = 2 for D1 ΔXp. *P* values (two-way ANOVA): (****) $P \leq 0.0001$, (*) $P \leq 0.05$ and NS implies nonsignificant. (*H*) Box plots representing the quantification of sphericity and the area occupied by *Xist* clouds in WT EV clones and clones with paternal D1 deletion. *P* values (Mann–Whitney *U* test): (****) $P \leq 0.0001$. n = 113, 100, 110, 100, 103.

Additionally, it has been shown that this region contains the P0 *Xist* promoter, although the existence of the P0 promoter remained controversial (Johnston et al. 1998; Warshawsky et al. 1999). Taken together, we hypothesized that this region may harbor regulatory elements that may be involved in the regulation of *Xist* and XCI. To test our hypothesis, we deleted the *Xist* upstream sequences (~6 kb) lying between *Tsix* and *Jpx* without interrupting *Xist*, *Tsix*, and *Jpx* using the CRISPR-Cas9 tool in XEN cells (Fig 2A, B). We generated two heterozygous XEN cell lines with paternal deletion (D1 ΔXp.1, D1 ΔXp.2) and three heterozygous clones with maternal allele deletion (D1 ΔXm.1, D1 ΔXm.2, D1 ΔXm.3) using CRISPR-Cas9 (Fig. 2B). The paternal or maternal deletions were verified through SNP-based Sanger sequencing (Supplemental Fig. S2A,B). We also generated empty-vector transfected clonal lines (WT EV1, WT EV2, and WT EV3) and WT XEN clonal lines (WT clone) for our experiments. Through RNA-seq analysis, we observed upregulation of *Xist* in paternally deleted clonal lines (D1 ΔXp) compared to both WT clones and WT EV clones ($\log_2$ FC > 2.4; FDR ≤0.01) (Fig. 2C). Reverse transcription quantitative-PCR (RT-qPCR) analysis, also showed significant upregulation of *Xist* in paternally deleted clonal lines (D1 ΔXp) compared to the WT EV clones (Fig. 2D). However, in maternally deleted clonal lines (D1 ΔXm), we did not observe such significant upregulation of *Xist* (Fig. 2D). However, through RNA-seq analysis, we observed moderate upregulation of *Xist* upstream regulators *Jpx* ($\log_2$ FC > 1; FDR ≤0.05), *Ftx* ($\log_2$ FC > 0.5; FDR ≤0.2), and *Rlim* ($\log_2$ FC > 1.5; FDR ≤0.01) in D1 ΔXp cells compared to both WT clones and WT EV clones (Fig. 2E). Of note, we did not notice such an increase in expression for *Jpx, Ftx*, and *Rlim* in RT-qPCR analysis (Supplemental Fig. S2C). Additionally, the expression of *Chic1*($\log_2$ FC > 3; FDR ≤0.01), a gene located in the adjacent *Tsix*-TAD, increased in D1 ΔXp clones (Supplemental Fig. S2D). Next, we performed RNA fluorescence in-situ hybridization (RNA-FISH) analysis for *Xist* in WT EV, D1 ΔXp, and D1 ΔXm XEN cells. We found a huge upregulation of *Xist* and dispersal of *Xist* clouds (~31%–42% cells) in D1 ΔXp lines (Fig. 2F,G). Investigation of these dispersed clouds showed multiple discrete *Xist* foci that spread along a large area of the nucleoplasm. However, the D1 ΔXm or the WT EV clones did not show this kind of *Xist* dispersal (Fig. 2F,G). Additionally, a significant percentage of cells in D1 ΔXp showed faint *Xist* clouds (Fig. 2F,G). Next, we compared the area and the sphericity of the dispersed *Xist* of D1 ΔXp lines with the compact *Xist* of WT EV clones and found that, whereas the area of the dispersed *Xist* clouds of the D1 ΔXp increased significantly, the sphericity of the clouds became significantly lower (Fig. 2H). Collectively, our analysis revealed that the deletion of the *Xist* upstream region leads to the upregulation of *Xist* expression and dispersal of *Xist* clouds.

Next, to further explore, we generated XEN cell lines with two segmental deletions (D2: near to *Xist*, and D3: near to *Jpx*) of the *Xist* upstream region using CRISPR-Cas9 (Fig. 3A). We generated heterozygous clones having deletion from either paternal or maternal allele for each of the D2 and D3 deletions. We validated heterozygous deletions through PCR followed by Sanger sequencing (Fig. 3B,C; Supplemental Fig. S3A–D). We also obtained homozygous clones for the D3 deletion (D3 ΔXpΔXm.1 and D3 ΔXpΔXm.2) (Fig. 3C; Supplemental Fig. S3D). Next, we performed RNA-FISH for *Xist* in the D2- and D3-deleted XEN cell clones. We found that deletion of the region near *Jpx* (D3) on the inactive X allele leads to the dispersal of *Xist* clouds to an almost similar extent (~32%–40% nuclei) as was observed in D1 ΔXp (Fig. 3E,F). D3 homozygous deletion also showed a similar phenotype (Fig. 3E,F). Accordingly, the dispersed *Xist* clouds of D3 homozygous and paternally deleted clones exhibited greater area and decreased sphericity compared to the compact *Xist* clouds of WT clones (Fig 3G). In converse, D3 deletion from the maternal/active X allele did not lead to such defects, suggesting the *cis*-effect of D3 deletion towards the *Xist* dispersal (Fig. 3E,F). RNA-FISH analysis also indicated the upregulation of *Xist* expression in D3 homozygous and paternally deleted clones (Fig. 3E). Consistent with this result, RNA-seq analysis of D3 homozygous clones revealed significant upregulation of *Xist* expression compared to both WT clones and WT EV clones ($\log_2$ FC > 1.2; FDR ≤0.01) (Fig. 3H). RT-qPCR analysis also showed an increase in the expression of *Xist* in D3 homozygous and paternally deleted clones (Fig. 3I). However, the D2 deletion from paternal/inactive X or the maternal/active X allele did not show such *Xist* upregulation or dispersal (Fig. 3D; Supplemental Fig. S4A). Collectively, our analysis suggested that the *Xist* upstream sequence near *Jpx* recapitulates the *Xist* upregulation and dispersal phenotypes as observed in D1 ΔXp.

On the other hand, through RNA-seq analysis, we found that there was a moderate increase in expression of *Jpx* ($\log_2$ FC > 1.4; FDR ≤0.01), *Ftx* ($\log_2$ FC > 1; FDR ≤0.01), and *Rlim* ($\log_2$ FC > 1; FDR ≤0.05) in D3 ΔXpΔXm cells compared to the WT clones and WT EV clones (Fig. 3J; Supplemental Fig. S4C). However, RT-qPCR analysis did not show such an increase in expression for *Ftx* and *Rlim*, but the expression of *Jpx* was found to be higher in D3 ΔXpΔXm cells (Supplemental Fig. S4B). We did not observe any considerable changes in expression for *Jpx*, *Ftx*, and *Rlim* in any of the D2-deleted lines (Supplemental Fig. S4A). Separately, the expression of *Chic1*($\log_2$ FC > 2; FDR ≤0.01), a gene located within the *Tsix*-TAD, was found to be increased in D3 homozygous XEN cells, consistent with what was found for the D1 ΔXp lines (Supplemental Fig. S4C).

Xist dispersal leads to the loss of repressive chromatin marks on the inactive X

After initiation of XCI, many repressive chromatin marks such as H3K27me3, H2AK119ub, H4K20me, Macro H2A, etc., accumulate on the inactive X, which plays an important role in the maintenance of gene silencing. We investigated whether the dispersal of *Xist* clouds leads to any defects or loss of enrichment of these different repressive marks on the inactive X. To explore this, we performed immunofluorescence (IF) for these different marks, followed by RNA-FISH for *Xist* in WT, D1, and D3 XEN cells. As expected, we found that all these marks are robustly enriched on the inactive X in WT XEN cells (Fig. 4). However, we observed that, whereas ~90% of WT XEN cells nuclei have robust enrichment of H3K27me3, there was a loss of enrichment of H3K27me3 in nuclei having dispersed *Xist* in D1 ΔXp, D3 ΔXp, and D3 ΔXpΔXm XEN cells (Fig. 4A). However, compact *Xist* coated nuclei in these cells maintained robust enrichment of H3K27me3 (Fig. 4A). Altogether, our data suggested that dispersal of the *Xist* cloud in D1 ΔXp, D3 ΔXp, and D3 ΔXpΔXm XEN cells leads to loss of H3K27me3 enrichment. Notably, H2AK119ub was still robustly enriched in *Xist*-dispersed nuclei of D1 ΔXp, D3 ΔXp, and D3 ΔXpΔXm XEN cells similar to the compacted *Xist* nuclei (Fig. 4B). On the other hand, enrichment of H4K20me1 was lost in ~90% of nuclei with the dispersed *Xist* cloud in D1 ΔXp, D3 ΔXp, and D3 ΔXpΔXm XEN cells (Fig. 4C). Additionally, whereas cells having compact *Xist* clouds retained strong and localized enrichment of MacroH2A.1, cells having dispersed *Xist* clouds possessed only an impression of faint and diffused MacroH2A.1, implying that proper *Xist* coating on the inactive X is critical for

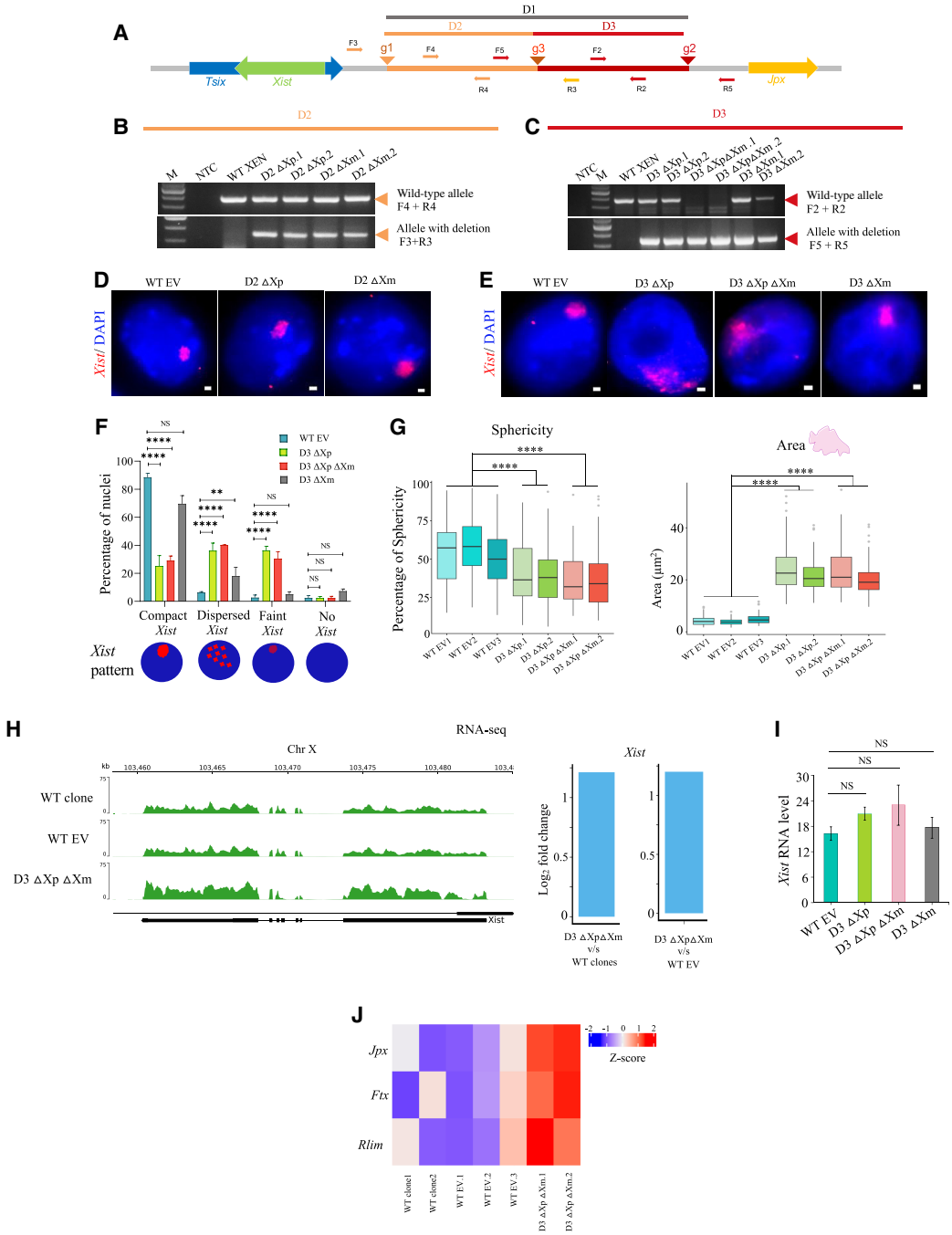

Figure 3. Segmental deletions of the *Xist* upstream sequence. (*A*) Schematic showing the segmental deletions (D2 and D3) regions upstream of *Xist*. Guide RNA target sites are represented as arrowheads (g1 and g3) for the D2 deletion and as arrowheads (g3 and g2) for the D3 deletion. Primer pairs are shown as orange and red arrows, F3 and R3 amplify the deleted allele, and F4 and R4 amplify the wild-type allele of the D2 deletion. F2 and R2 amplify the undeleted allele, and F5 and R5 amplify the deleted allele of the D3 deletion. (*B*) PCR-based identification of D2 paternally (D2 ΔXp.1 and D2 ΔXp.2) and maternally deleted clones (D2 ΔXm.1 and D2 ΔXm.2). Orange arrows mark the position of the expected amplicons. M denotes marker and NTC: no template control. (*C*) PCR for the paternally (D3 ΔXp.1 and D3 ΔXp.2), homozygous (D3 ΔXp ΔXm.1 and D3 ΔXp ΔXm.2) and maternally (D3 ΔXm.1 and D3 ΔXm.2) deleted lines of the D3 deletion. Red arrowheads mark the position of the amplicons. The primers used for each PCR are indicated on the *right*. (*D*) RNA-FISH for WT EV and D2 deletion clones using double-stranded *Xist*/*Tsix*-Cy3 (red) probe. Nuclei are counterstained with DAPI (blue). Scale bars: 1 µm. (*E*) RNA-FISH using double-stranded DNA probe for *Xist*/*Tsix*-Cy3 (red) in WT EV, D3 ΔXp, ΔXpΔXm, and ΔXm clones. Scale bars: 1 µm. (*F*) Quantification of the pattern of different *Xist* coating in the D3 deleted clones. n = 3 for WT EV clones and n = 2 for each of D3 ΔXp, D3 ΔXpΔXm, and D3 ΔXm clones. *P* values (two-way ANOVA): (****) $P \leq 0.0001$, (**) $P \leq 0.01$. (*G*) Quantification of the sphericity and area occupied by the *Xist* clouds in the D3 deleted (homozygous and paternally deleted) clonal lines and WT EV clones. *P* values (Mann–Whitney *U* test): (****) $P \leq 0.0001$. n = 113, 100, 110, 99, 102, 98, 97. (*H*) *Left*: Genome browser view of *Xist* expression for WT clones, WT EV and D3 ΔXpΔXm clones as obtained from RNA-seq. *Right*: Bar plots representing the $\log_2$ fold change for *Xist* in D3 ΔXpΔXm over WT clone and WT EV clones. (*I*) RT-qPCR for analysis of *Xist* expression levels normalized to *Tbp* for the D3 deleted lines. (*J*) Heat map showing the increased expression of *Jpx*, *Ftx*, and *Rlim* in D3 ΔXpΔXm cells compared to the WT clone and WT EV clones.

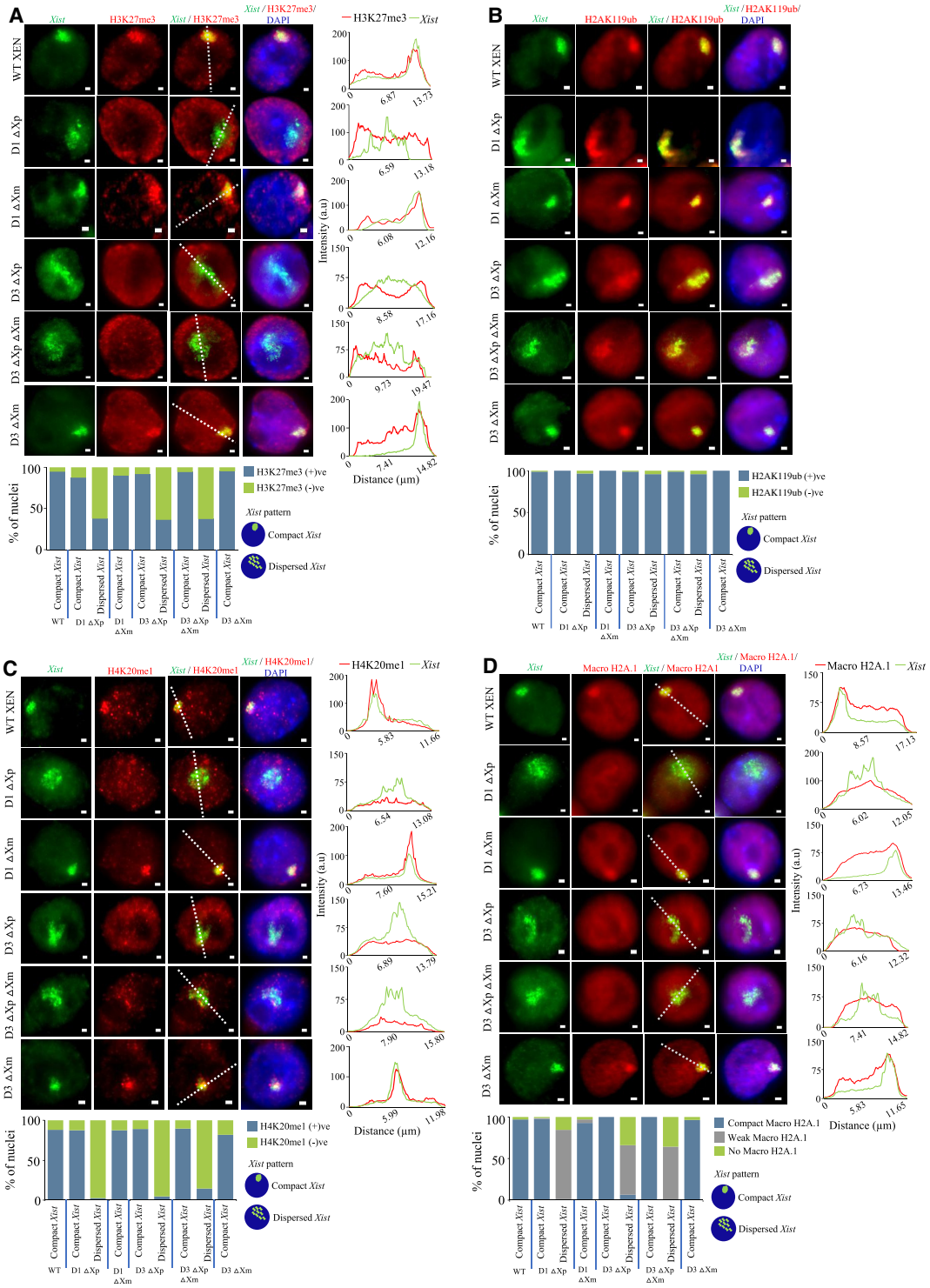

Figure 4. *Xist* dispersal is associated with the loss of enrichment of repressive chromatin marks on the inactive X. (*A*) Representative images of IF-RNA FISH of H3K27me3 (red) and *Xist* (green) for WT XEN, D1 ΔXp, D1 ΔXm, D3 ΔXp, D3 ΔXp ΔXm, and D3 ΔXm lines. *Right*: Corresponding fluorescent intensity profiles for *Xist* and H3K27me3 along the white line drawn across the *Xist* cloud. *Bottom*: Quantification of the enrichment of H3K27me3 on the inactive X in compact and dispersed *Xist* nuclei. n = 129, 108, 66, 96, 112, 105, 132, 100, 145 (for each data point from *left* to *right*). (*B*) Representative IF-RNA FISH images for H2AK119ub (red) and *Xist* (green) for D1 and D3 deleted lines. *Bottom*: Quantification of the the enrichment of H2AK119ub on the inactive X in compact and dispersed *Xist* nuclei. n = 120, 123, 128, 126, 108, 146, 135, 127, 116 (for each data point from *left* to *right*). (*C*) IF-RNA FISH images with corresponding intensity profiles for H4K20me1 (red) and *Xist* (green). *Bottom*: Quantification for enrichment of H4K20me1 in compact and dispersed *Xist* nuclei. n = 137, 153, 135, 155, 131, 141, 133, 129, 143 (for each data point from *left* to *right*). (*D*) Macro H2A.1 (red) and *Xist* (green) IF-RNA FISH representative images with their corresponding intensity profiles are shown. *Bottom*: Quantification of compact, weak, and no Macro H2A.1 signals in nuclei having compact and dispersed *Xist* clouds in the D1 and D3 deleted lines. n = 120, 158, 137, 138, 116, 106, 110, 109, 135 (for each data point from *left* to *right*). A single-stranded RNA probe was used to detect *Xist*.

the association of MacroH2A.1 (Fig. 4D). Taken together, our analysis suggested that *Xist* dispersal in D1 ΔXp, D3 ΔXp, and D3 ΔXpΔXm XEN cells leads to loss of H3K27me3, H4K20me1, and MacroH2A enrichment on the inactive X. However, H2AK119ub enrichment remains robustly maintained.

Xist dispersal does not affect the nucleolar association of the inactive X

Next, we explored whether the dispersal of *Xist* and loss of different repressive chromatin marks leads to the perturbation of nucleolar association of the inactive X. The inactive X is known to primarily occupy two regions of the nucleus—one in association with the nucleolus and the other in close proximity to the nuclear membrane (Zhang et al. 2007). The association of the inactive X to the nucleolus primarily occurs during the maintenance phase of XCI, and it is believed that nucleolar association helps to maintain the heterochromatin state of the inactive X. It is thought that nucleolar association of the inactive X is primarily facilitated by the *Xist* RNA, and upon loss of *Xist*, the inactive X has been found to dissociate from the nucleolus (Zhang et al. 2007; Kelsey et al. 2015). Therefore, to test whether the inactive X loses its nucleolar association upon *Xist* dispersal, we performed IF staining for fibrillarin (a protein that is a part of the fibrillar matrix of the nucleolus) to mark the nucleolus, followed by RNA-FISH for *Xist* (Fig. 5A). The *Xist* clouds were quantified by categorizing the signals to be associated with only the nucleolus, or to the nuclear membrane, or to both the nucleolus and the nuclear membrane, or neither of them (Fig. 5A). We found that the dispersed *Xist* clouds of the D1 ΔXp, D3 ΔXp, and D3 ΔXpΔXm XEN cells were associated to the nucleolus similarly as the compact *Xist* clouds of the WT or the maternally deleted lines (Fig. 5A). Taken together, our analysis suggested that inactive X remains associated with the nucleolus despite *Xist* dispersal and loss of repressive marks.

Xist-tethering proteins remain enriched on the inactive X of the *Xist*-dispersed nuclei

Next, we wanted to find out if the dispersal of *Xist* is because of the loss of proper enrichment of *Xist*-tethering proteins, such as CELF1, CIZ1, etc., upon *Xist* upstream deletion. CELF1 has been identified as a key protein that forms a heterochromatic assembly that maintains proper *Xist* localization, and its loss results in *Xist* disassociation from the inactive X (Pandya-Jones et al. 2020). We first looked at the CELF1 enrichment in the D1 deletion lines that displayed *Xist* dispersal using IF staining for CELF1 coupled with *Xist* RNA-FISH but did not find any noticeable defect in the CELF1 enrichment in such nuclei (Fig. 5B). This implied that *Xist* dispersal was not a consequence of alteration in CELF1 enrichment levels. Next, we looked into the enrichment of another tethering protein, CIZ1, that establishes very strong interaction with the *Xist* RNA and keeps it stably associated with the inactive X (Ridings-Figueroa et al. 2017). We performed similar experiments for the CIZ1 protein and found that CIZ1 also remained associated with dispersed *Xist* clouds in paternally deleted D1 lines (Fig. 5C). Altogether, our analysis suggested that the dispersal of *Xist* clouds was not associated with the loss of tethering proteins.

Xist upstream deletion does not perturb X-linked gene silencing but affects autosomal gene expression

As we observed loss of enrichment of several repressive marks (H3K27me3, H4K20me1, and MacroH2A) on the inactive X of dispersed *Xist* nuclei, it intrigued us to explore the status of X-linked gene silencing on the inactive X. For this, we performed allele-specific RNA-seq analysis for the WT clones, WT EV clones, D1 ΔXp, and D3 ΔXpΔXm XEN cells. As expected, both in WT clones and WT EV clones, X-linked genes showed exclusive expression from the maternal active X (X^{Mol}), except for a few escapee genes (Fig. 6A). In D1 ΔXp, and D3 ΔXpΔXm cells as well, the majority of the X-linked genes expression originated exclusively from the maternal active X (X^{Mol}), suggesting that the inactive X still maintained X-linked gene silencing in these cells despite the loss of repressive marks and *Xist* dispersal (Fig. 6A). Notably, four genes (*Arhgap6, Hccs, Zrsr2, Syap1*) appeared to be reactivated in D1 ΔXp and D3 ΔXpΔXm XEN cells compared to WTEV clones. However, they exhibited an escapee expression pattern in WT clones (Fig. 6A). Because RNA-seq gave us insight only about the bulk expression profile of the X-linked genes, we wanted to check whether there was X-linked gene reactivation at the single-cell level through RNA-FISH. We performed RNA-FISH for three X-linked genes, namely: *Rlim*, *Atrx*, and *Pg*k1 coupled with *Xist* (Fig. 6B). As expected, WT-XEN cells showed monoallelic expression for all three X-linked genes. Dispersed *Xist* nuclei in D1 ΔXp and D3 XpXm XEN cells maintained monoallelic expression of the X-linked genes similar to the compact *Xist*-coated nuclei (Fig. 6B). Taken together, our analysis suggested that X-linked genes remained silent on the inactive X, despite *Xist* dispersal or loss of repressive marks. Although there was no effect on inactive X gene silencing, we explored if there was any effect on autosomal gene expression. Many autosomal genes showed differential expression ($\log_2$ FC > 2; FDR <0.01) in D1 ΔXp and D3 ΔXpΔXm XEN cells, compared to both WT clones and WT EV clones (Fig. 6C,D; Supplemental Table S2). Notably, the differentially expressed genes in *Xist* upstream deleted clones showed a high level of similarity (77% –93%) when compared to both WT clones and WT EV clones, confirming the accuracy of our analysis (Fig. 6C,D; Supplemental Fig. S5A). Moreover, many upregulated or downregulated genes were common between D1 ΔXp and D3 ΔXpΔXm XEN cells (Supplemental Fig. S5B). Accordingly, Gene Ontology analysis of differentially expressed genes showed enrichment of genes in many common biological processes between D1 ΔXp and D3 ΔXpΔXm XEN cells, such as chromatin organization, chromatin remodeling, chromosome organization, metabolic processes, etc. (Supplemental Fig. S5D). Importantly, we observed the upregulation of *Rad21* in D1 ΔXp ($\log_2$ FC > 1.3; FDR ≤ 0.01), and D3 ΔXpΔXm XEN cells ($\log_2$ FC > 0.6; FDR ≤ 0.12) compared to both WT clones and WT EV clones (Fig. 6E; Supplemental Fig. S5C). Collectively, we conclude that *Xist* upstream deletion is associated with the alterations of autosomal gene expression.

Deletion of *Xist* upstream sequence leads to the alterations of topological contacts of *Xist* and genome-wide CTCF/RAD21 occupancy

Next, we investigated whether the deletion of *Xist* upstream sequences on the inactive X affects the spatial contacts of the *Xist* locus. To explore this, we performed allele-specific 4C-seq on paternally deleted lines (D1 ΔXp.1, D1 ΔXp.2) and WT XEN. From the viewpoint at the *Xist* locus, we found alterations of contacts of *Xist* with the regions encompassing *Ftx* in the inactive X Chromosome in D1 ΔXp cells (Fig. 7A; Supplemental Fig. S6A). Notably, we observed more gains of contact than loss between *Xist* and the *Ftx* loci in D1 ΔXp cells compared to the WT (Fig. 7A). Concordant with the increased contacts between *Xist* and

Ftx loci in D1ΔXp cells, we found increased occupancy of RAD21 encompassing the *Xist* and *Ftx* loci (Fig. 7B). On the other hand, we observed loss of few CTCF peaks at these loci (Fig. 7C). Taken together, we conclude that deletion of *Xist* upstream sequence on the inactive X in D1 ΔXp cells leads to major alterations in contacts between the *Xist* and *Ftx* loci and CTCF/RAD21 occupancy

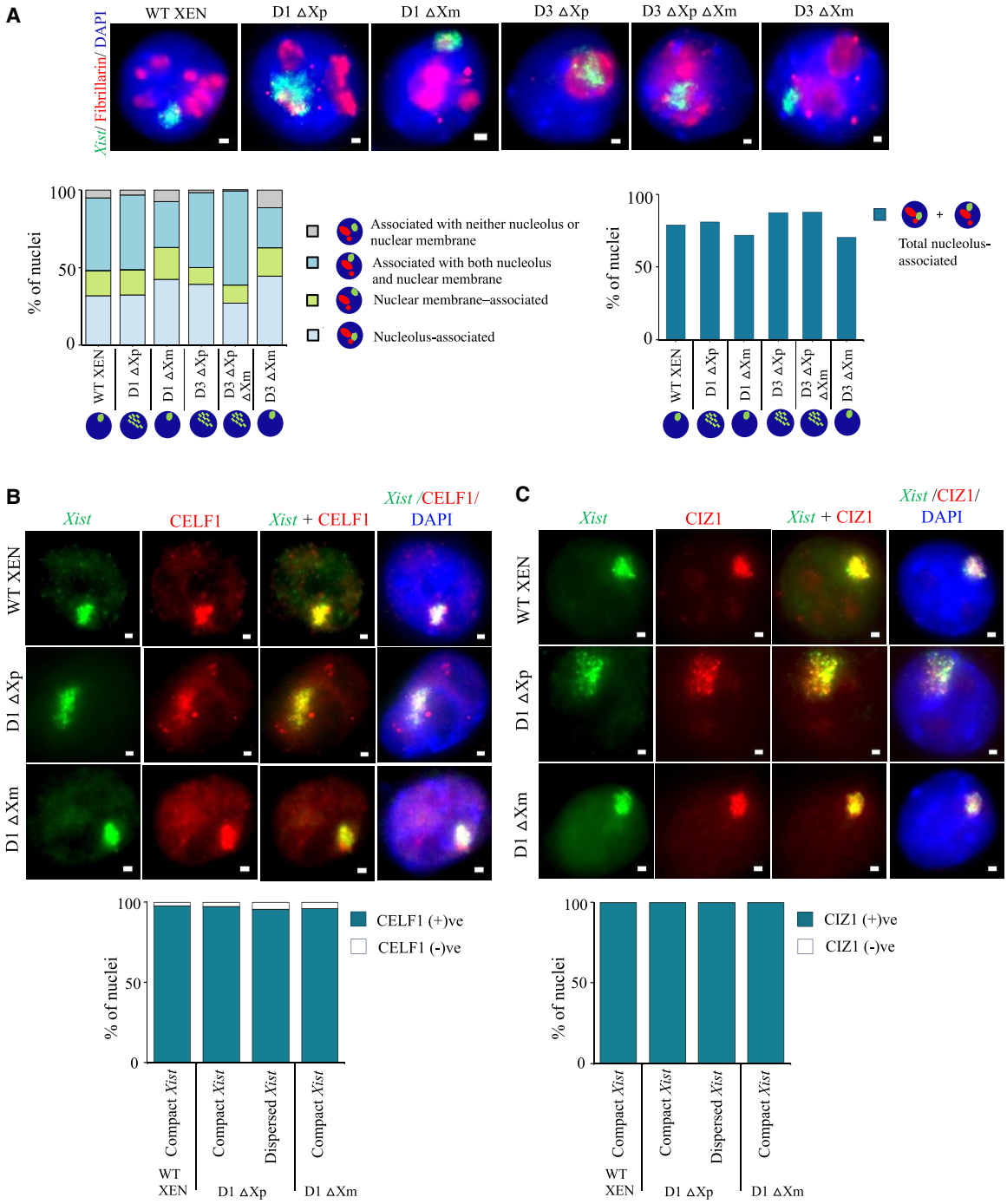

Figure 5. *Xist*-dispersed nuclei retains association with the nucleolus and do not show alteration in CELF1 and CIZ1 enrichment. (*A*) *Top*: Representative images of IF-RNA FISH for fibrillarin (red) and *Xist* (green) in WT, D1, and D3 deleted lines. *Bottom*:Quantification of the association between *Xist* cloud and fibrillarin signals in nuclei with compact and dispersed *Xist* clouds in the D1 and D3 deleted lines. n = 119, 157, 146, 120, 122, 148 (for each data point from *left* to *right*). Quantifications were performed based on single Z-planes. (*B*) Representative images for IF-RNA- FISH for CELF1(red) and *Xist* (green) in WT and D1 deleted lines. *Bottom*: Quantification of enrichment of CELF1 on the inactive X in compact versus dispersed *Xist* nuclei. n = 246, 110, 96, 101 (for each data point from *left* to *right*). (*C*) Images representing IF-RNA-FISH for CIZ1 (red) and *Xist* (green) in WT and D1 deleted lines. *Bottom*: Quantification of enrichment of CIZ1 on the inactive X in compact versus dispersed *Xist* nuclei. n = 128, 111, 120, 114 (for each data point from *left* to *right*). A single-stranded RNA probe was used to detect *Xist*.

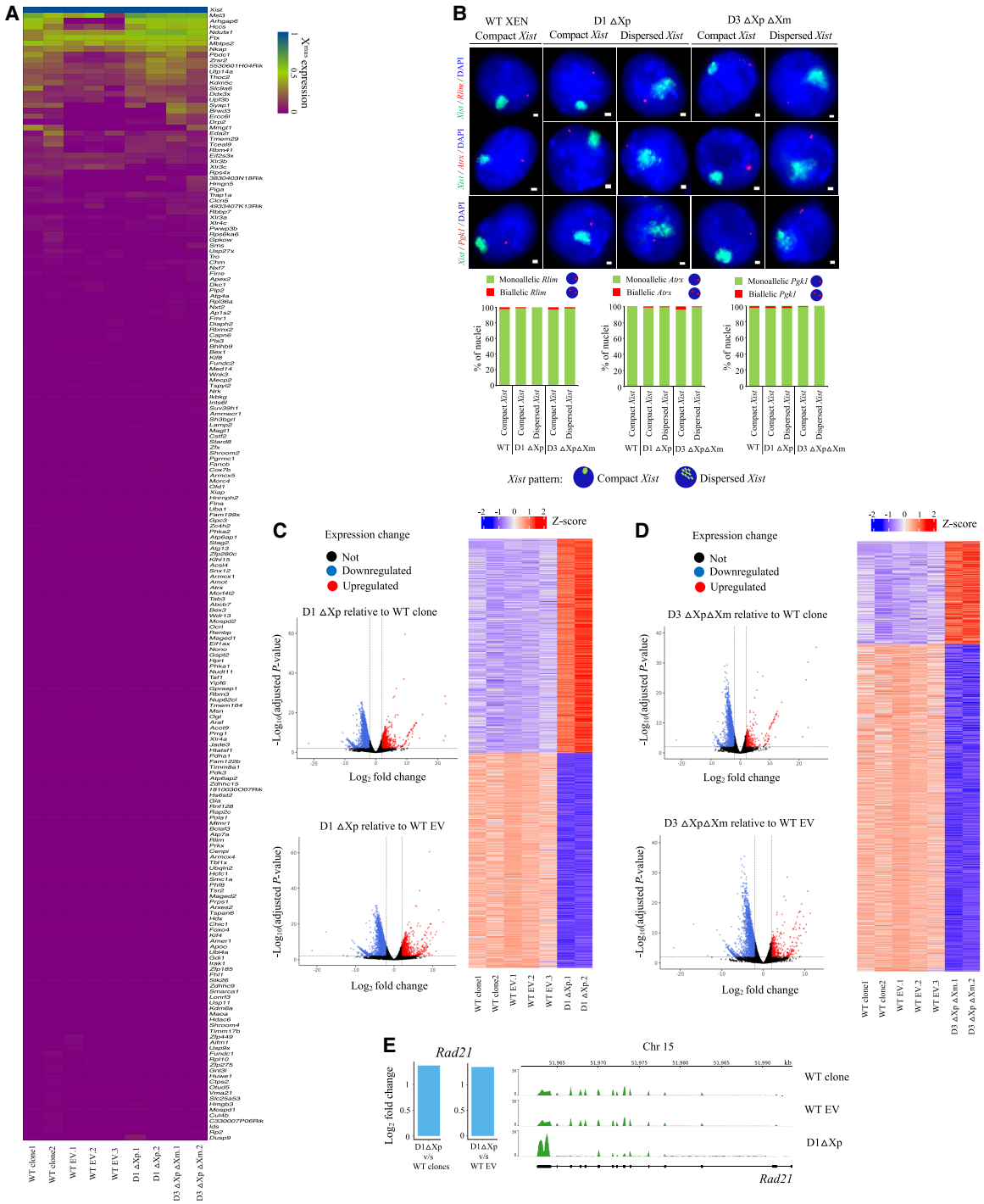

Figure 6. *Xist* upstream deletion affects autosomal gene expression. (*A*) Heat map showing the fraction allelic expression pattern of different X-linked genes for D1 ΔXp.1, D1 ΔXp.2, D3 ΔXpΔXm.1, and D3 ΔXp ΔXm.2 lines as compared to WT clones and WT EV clones (WT EV.1, WT EV.2, and WT EV.3). (*B*) Representative images of RNA-FISH for *Xist* (green) and X-linked genes *Rlim*, *Atrx*, and *Pgk1* (red) in WT and D1 and D3 deletion lines. *Bottom*: Quantification of mono/biallelic expression of *Rlim* (n = 109, 109, 86, 116, 126), *Atrx* (n = 103, 85, 101, 159, 136), or *Pgk1*(n = 117, 118, 102, 120, 88) in nuclei having compact versus dispersed *Xist* clouds. A single-stranded RNA probe was used to detect *Xist*. (*C*) *Left*: Volcano plots representing the differentially expressed genes in D1 ΔXp relative to WT clones and WT EV clones (DESeq2: $\log_2$ FC > 2; FDR < 0.01). *Right*: Heat map showing the top differentially expressed genes in D1 ΔXp relative to WT clones and WT EV clones. (*D*) *Left*: Volcano plots representing the differentially expressed genes in D3 ΔXpΔXm relative to WT clones and WT EV clones (DESeq2: $\log_2$ FC > 2; FDR <0.01). *Right*: Heat map showing the differentially expressed genes in D3 ΔXpΔXm relative to WT clones and WT EV clones. (*E*) *Left*: Plots showing fold changes of *Rad21* expression as seen through RNA-seq for D1 ΔXp lines as compared to WT clones and WT EV clones. *Right*: Genome browser views showing *Rad21* expression across the genomic loci for WT clone, WT EV, and D1 ΔXp lines.

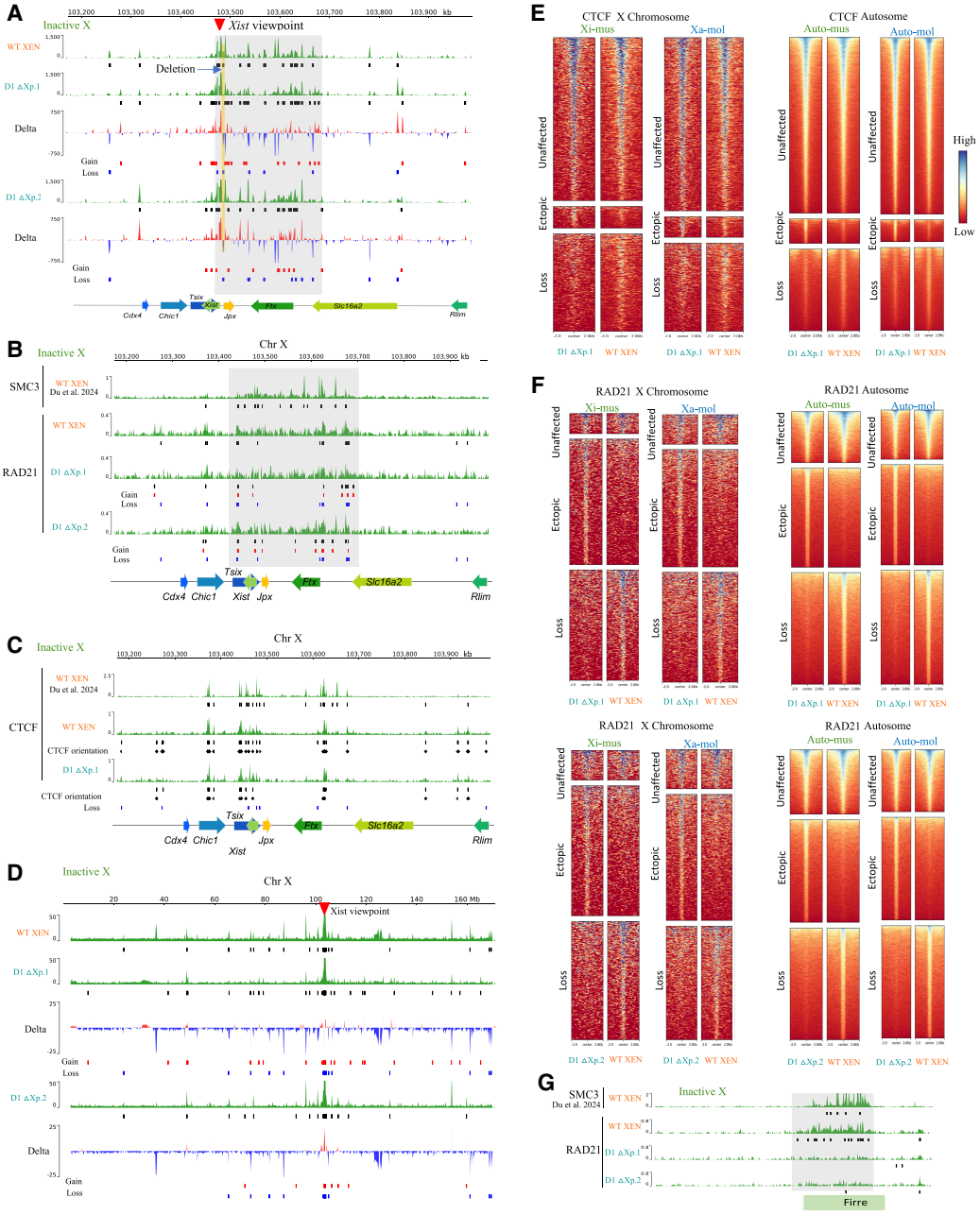

Figure 7. Deletion of *Xist* upstream sequences leads to genome-wide changes in *Xist* interaction and alterations of CTCF, RAD21 binding. (*A*) Xi-specific 4C interaction profiles of the *Xist* locus with genomic region across the *Xic* in WT XEN versus D1 ΔXp.1 (*top*) and WT versus D1 ΔXp.2 (*bottom*). The red arrow marks the viewpoint at the *Xist*. Black boxes *below* each track denote significant interactions. Delta plots represent the differences in interactions between WT versus D1 ΔXp cells. Gains and losses of interactions are marked through red and blue boxes, respectively. The shaded area highlights alterations of interactions between WT versus D1 ΔXp cells in the region encompassing the *Xist* and *Ftx* loci. Deleted region is marked by a yellow line. (*B*) Tracks showing the Xi-specific enrichment of SMC3 in WT XEN (*top*) and RAD21 in WT XEN and D1 ΔXp.1 and D1 ΔXp.2 (*bottom*). Black boxes denote significant peaks *under* each track. Gains and losses of significant peaks are marked through red and blue boxes, respectively. The shaded area highlights alterations of RAD21 binding between WT versus D1 ΔXp cells in the region encompassing the *Xist* and *Ftx* loci. Analysis of RAD21 is based on ChIP-seq and SMC3 is based on CUT&RUN. (*C*) Tracks showing the Xi-specific enrichment of CTCF in WT XEN versus D1 ΔXp.1. Black boxes *under* each track denote significant peaks. Gains and losses of significant peaks are marked through red and blue boxes, respectively. CTCF orientations are denoted through black arrowheads. Analysis of CTCF XEN ($Xi^{MOT}Xa^{Mus}$) is based on CUT&RUN; others are based on ChIP-seq. (*D*) Xi-specific 4C interaction profiles of the *Xist* locus across the inactive X in WT XEN versus D1 ΔXp.1 (*top*) and WT versus D1 ΔXp.2 (*bottom*). The red arrow marks the viewpoint. Black boxes *below* each track denote significant interactions. Delta plots represent the differences in interactions between WT versus D1 ΔXp cells. Gains and losses of interactions are marked through red and blue boxes, respectively. (*E*) Allele-specific enrichment plots showing unaffected, ectopic, or lost CTCF peaks across the X Chromosome (*left*) and autosome (*right*) in D1 ΔXp.1 versus WT XEN lines. (*F*) Allele-specific enrichment plots showing unaffected, ectopic, or lost RAD21 peaks across the X Chromosome (*left*) and autosome (*right*) in D1 ΔXp.1 versus WT XEN lines (*top*) and D1 ΔXp.2 versus WT XEN lines (*bottom*). (*G*) Tracks showing Xi-specific SMC3 and RAD21 enrichments across the *Firre* locus for WT XEN, D1 ΔXp.1, and D1 ΔXp.2 lines. Black boxes denote significant peaks *under* each track. The shaded area highlights alterations of RAD21 binding between WT versus D1 ΔXp cells across the *Firre* locus.

(Supplemental Tables S3, S4). Separately, we observed alterations of *Xist* locus contacts and CTCF and RAD21 occupancy in active X Chromosomes as well (Supplemental Fig. S6B–D).

Next, we investigated if the deletion of the *Xist* upstream sequence affects the long-range interactions of the *Xist* locus. We found that *Xist* has several long-range contacts across the inactive X beyond the *Xic* (Fig 7D; Supplemental Fig. S7B). Moreover, we observed major alterations of long-range interactions with the *Xist* locus throughout the inactive X in *Xist* upstream-deleted D1 ΔXp.1 and D1 ΔXp.2 cells (Fig 7D; Supplemental Table S4). Additionally, we found that there were changes in interchromosomal contacts in D1 ΔXp cells (Supplemental Figs. S7A, S8, and S9). Taken together, our analysis suggested that deletion of *Xist* upstream sequences on the inactive X not only impairs the contacts at the *Xic* but also affects the interaction of the locus across the X Chromosome and the genome. Next, we profiled the enrichment of CTCF and RAD21 in WT and *Xist* upstream-deleted D1 ΔXp cells. We found that the overall enrichment of CTCF and RAD21 on the inactive X was less than the active X Chromosome in WT cells (Supplemental Fig. S10A,B). As expected, allelic enrichment of CTCF/RAD21 on autosomes was equivalent, validating our allele-specific ChIP-seq analysis pipeline (Supplemental Fig. S10A, B). Notably, in D1 ΔXp cells, enrichment of CTCF and RAD21 on the inactive X was also less than the active X (Supplemental Fig. S10A,B). However, we found loss and gain of peaks for CTCF and RAD21 at many loci across the inactive X in D1 ΔXp cells compared to the WT cells (Fig 7E,F; Supplemental Table S3). It is known that the inactive X gets compartmentalized into two large megadomains that hinge at the microsatellite repeat region *Dxz4*. In addition, the inactive X harbors two superloops that include long-range high-frequency interactions between *Firre-Dxz4* and *Dxz4-x75* (Deng et al. 2015; Barutcu et al. 2018; Fang et al. 2020). Previous studies have demonstrated that CTCF/RAD21 is enriched at these superloop-forming loci and plays an important role in the formation of superloops (Barutcu et al. 2018; Froberg et al. 2018). Invariably, we found strong enrichment of CTCF and RAD21 in WT XEN cells at the *Firre* locus (Fig. 7G; Supplemental Fig. S11A, B). The occupancy of RAD21 at the *Firre* locus of the inactive X was drastically reduced in the D1 ΔXp XEN lines compared to the WT cells (Fig. 7G). However, we did not observe much alteration in the CTCF/RAD21 occupancy at *Dxz4* and *x75* loci (Supplemental Fig. S11C). Taken together, our analysis suggests that deletion of *Xist* upstream sequence on the inactive X leads to alterations of contacts of the *Xist* locus and binding of CTCF/RAD21 across the inactive X, indicating there could be impairment of superloop formation and overall conformational changes of the inactive X Chromosome in the D1 ΔXp XEN lines. Additionally, we observed alterations of CTCF/RAD21 occupancy across autosomes and the active X as well in D1 ΔXp cells (Fig. 7E,F; Supplemental Table S3).

Discussion

In this study, we have explored the contribution of *Xist* upstream elements in the regulation of *Xist* and XCI in XEN cells, which undergo imprinted XCI. We show that the *Xist* locus in XEN cells anchors interactions with the *Xist* upstream regulators on the inactive X similar to MEF cells with random XCI (Fig 1). Such interactions were reported previously in other cell types with random XCI (Nora et al. 2012; Galupa and Heard 2018; Galupa 2023; Poonperm et al. 2023). Importantly, we found that the major interactions were between the *Xist* and *Ftx* locus, which often coincided with the enrichment of CTCF and cohesin (RAD21 and SMC3) similar to that of the MEF cells with random XCI (Fig. 1; Supplemental Fig. S1D). However, we found few interactions of the *Xist* locus with the neighboring *Tsix*-TAD loci, suggesting the existence of inter-TAD interactions as reported previously (Fig. 1C; Despang et al. 2019; Galupa et al. 2020). Additionally, we observed the enrichment of enhancer marks H3K4me1 and H3K27ac in a region encompassing *Xist* to *Ftx* loci in XEN cells (Fig. 1F). However, such enrichment for H3K27ac was absent in MEF cells having random inactive X (Fig. 1F).

Next, we investigated the role of an ~6-kb region upstream of *Xist*, located between *Tsix* and *Jpx*, in regulating *Xist* and XCI. We demonstrate that the deletion of these *Xist* upstream sequences in the inactive X in XEN cells leads to the upregulation of *Xist* expression as well as the dispersal of *Xist* clouds (Fig. 2). A series of studies have deleted the different *Xist* activators (*Jpx, Ftx, Xert, Rlim*) located upstream of *Xist* and explored the effect on *Xist* regulation and XCI (Shin et al. 2010, 2014; Tian et al. 2010; Barakat et al. 2014; Wang et al. 2016; Furlan et al. 2018; Hosoi et al. 2018; Collombet et al. 2020; Gjaltema et al. 2022; Ravid Lustig et al. 2023). Additionally, deletion of an ~2.5-kb region in ES cells encompassing two DHSs located at around 1.4 kb and 3 kb upstream of the *Xist* TSS, respectively, did not result in any phenotype (Newall et al. 2001; Clerc and Avner 2003). Taken together, whereas many upstream regulators of *Xist* have been perturbed to date, no study has explored the effect of the deletion of the *Xist* upstream sequence lying between *Tsix* and *Jpx* reported in our study. Therefore, our deletion analysis of this region provides significant and novel insights related to regulating *Xist* and XCI.

On the other hand, we observed loss of enrichment of different repressive marks from the inactive X, such as H3K27me3, H4K20me1, and MacroH2A.1, in *Xist*-dispersed nuclei (Fig 4). This indicated that recruitment of such marks may require the proper *Xist* cloud formation. However, H2AK119ub was still found to be strongly enriched on the inactive X of nuclei with dispersed *Xist*, suggesting that enrichment of H2AK119ub is not dependent on proper compact coating of *Xist* (Fig 4). Our result is consistent with a recent study showing that, during the initiation of XCI, H2AK119ub is enriched even before *Xist* gets accumulated in a compact manner on the inactive X (Valledor et al. 2023). Furthermore, our results support the finding that PRC2-mediated H3K27me3 is directly recruited by *Xist* RNA and might not always be dependent on PRC1 for its recruitment, as a result of which dispersal of *Xist* contributes to the loss of PRC2 recruitment (Cifuentes-Rojas et al. 2014; Davidovich and Cech 2015). On the other hand, there was no alteration in nucleolar association of the inactive X despite *Xist* dispersal and loss of repressive mark enrichment (Fig. 5A). It is believed that CTCF and cohesin binding at the *Firre* locus is important for perinucleolar localization of the inactive X (Yang et al. 2015). However, we find that loss of cohesin (RAD21) at the *Firre* locus in *Xist* upstream-deleted cells did not affect the perinucleolar localization of the inactive X, suggesting cohesin at the *Firre* locus may be dispensable for nucleolar localization of the inactive X (Fig. 7G). In this respect, the *Xist* RNA might itself be sufficient to recruit the inactive X to the nucleolus independent of the cohesin binding at the *Firre* locus (Zhang et al. 2007). Separately, we found that *Xist*-tethering proteins such as CELF1 and CIZ1 were still robustly enriched in *Xist*-dispersed nuclei, indicating that enrichment of tethering proteins is not sufficient for proper *Xist* coating (Fig. 5B,C). Notably, despite *Xist* dispersal and loss of enrichment of repressive marks, genes on the inactive X remained silent (Fig. 6A). However,

we observed dysregulation of autosomal gene expression in these cells (Fig. 6C,D).

We found that the *Xist* locus has long-range contacts across the inactive X as described previously (Fig. 7D; Splinter et al. 2011; Galupa et al. 2020). We observed alterations of contacts of the *Xist* locus across the inactive X and autosomes in D1 ΔXp cells (Fig. 7D; Supplemental Figs. S8, S9). We think such alterations of contacts can be attributed to the global alterations of CTCF/RAD21 occupancy in D1 ΔXp cells (Fig. 7E,F). We believe that the upregulation of expression of cohesin *Rad21* alters global cohesin occupancy in D1 ΔXp cells and thereby leads to such contact alterations. In fact, previous studies reported that the upregulation of cohesins is associated with alterations of topological contacts (Sun et al. 2023). Dispersed *Xist* RNA in D1 ΔXp cells can bind to the other loci at autosomes, which can also alter the CTCF and cohesin binding. Indeed, previous studies reported that *Xist* can evict the cohesin protein from the inactive X Chromosome (Minajigi et al. 2015). Separately, contact alterations in D1 ΔXp cells can be linked to dysregulation of numerous genes related to chromosome organization (Supplemental Fig. S5D). On the other hand, we see variations in interactions among the clones. This can be attributed to the variations in breakpoints among the *Xist* upstream deleted clones (Supplemental Fig. S2B) as well as to variation in the extent of *Rad21* upregulation among clones. It is worth discussing that one of the limitations of our 4C analysis is that it lacks biological replicates for WT XEN cells. Separately, we observed an alteration of contacts between the *Xist* and *Ftx* loci in D1 ΔXp cells. We found more gain of interactions than loss between these loci (Fig. 7A). Notably, there was a greater gain of RAD21 enrichment in these loci as well (Fig. 7B). We observed the loss of a few CTCF peaks at *Xist* and *Ftx* loci in the inactive X of deleted cells (Fig. 7C). Taken together, we conclude that most likely alterations of CTCF/RAD21 occupancy at the *Xist* upstream locus leads to the alterations of *Xist* locus interactions. However, we noticed that the loss or gain of interactions did not overlap with the loss or gain of CTCF/RAD21 binding. The upregulation of *Xist* in D1 ΔXp cells could be attributed to these topological changes. Indeed, it has been shown that topological alterations can lead to dysregulation of transcription of genes at *Xic* (Nora et al. 2012; van Bemmel et al. 2019). Alternatively, it is also possible that expression changes of *Xist* and other transcripts in that region altered the topological interactions. Whether the alterations in the topological contacts are a cause or an effect of the observed transcriptional changes remains an open question. Separately, changes in *Xist* expression could be due to the *Xist* locus becoming closer to *cis*-regulatory elements upon deletion of *Xist* upstream sequence.

Next, we observed substantial loss of RAD21 enrichment at the *Firre* locus, which is known to be involved in the inactive X superloop formation, indicating that there could be destabilization of superloops, as diminished CTCF/RAD21 binding has been shown to lead to loss of chromatin contacts (Fig. 7G). Importantly, superloops on the inactive X are essential for maintaining the 3D structure and the inactive X packaging; therefore, destabilization of the superloops can lead to the deformation of the 3D structure of the inactive X (Darrow et al. 2016). It is possible that conformational changes of inactive X upon deletion of *Xist* upstream sequence leads to the dispersal of *Xist*. Indeed, previous reports have shown that spreading and coating of *Xist* RNA depend on the structure and the spatial configuration of the X Chromosome (Chen et al. 2016). *Xist* has been shown to make use of specific "entry sites" at the inactive X, which are topologically proximal to its locus of transcription, to bind and spread across the whole X Chromosome (Boeren and Gribnau 2021). The changes in the spatial conformation of the *Xic* and also the whole X Chromosome can be speculated to have affected *Xist*'s search for its entry sites, which led to the dispersal of *Xist*. Alternatively, the *Xist* upregulation and dispersal of *Xist* may lead to alterations in the topological conformation of the *Xic* and X Chromosome. Separately, *Xist* dispersal could be attributed to the upregulation of *Xist* expression. Indeed, previous studies reported that overexpression of *Xist* leads to the spreading of *Xist* beyond the X Chromosome, which appears to be in the form of discrete foci concomitant to what we have observed (Jachowicz et al. 2022). On the other hand, segmental deletions of the *Xist* upstream region revealed that the deletion of *Xist* upstream sequence near *Jpx* (D3) recapitulates the *Xist* upregulation and dispersal phenotypes as observed in D1 deletion (Fig. 3). We believe that D2 and D3 harbor different genomic or epigenomic elements, which can contribute to these phenotypic differences. Indeed, D2 and D3 regions differ in terms of enrichment of LINEs, DHSs, pseudogenes, and promoter elements (*Xist* P0: belongs to D3) (Supplemental Fig. S4D). Moreover, enrichment of H3K9me3 appeared to be higher in D3 compared to D2, although peaks were not significant (Supplemental Fig. S4D). Another possibility is that D2 deletion might have no effect on the topological interactions between *Xist* and *Ftx* loci, and thereby, it does not affect *Xist* regulation. In the future, it will be interesting to investigate the mechanism underlying these differences in phenotypic outcomes between D2 and D3 deletions. Separately, we propose that autosomal dysregulation could be due to several reasons, such as (1) binding of dispersed *Xist* RNA at other autosomal loci, affecting their expression through recruitment of silencing proteins, (2) genome-wide alterations of CTCF and cohesin occupancy and associated topological interactions, or (3) dysregulation of genes involved in chromatin remodeling and chromatin organization. Indeed, a recent study demonstrated that dispersed *Xist* can affect autosomal gene expression (Dror et al. 2024). Taken together, our study reveals that the deletion of the *Xist* upstream sequences located between *Tsix* and *Jpx* leads to diverse outcomes such as upregulation of *Xist*, dispersal of *Xist* clouds, loss of repressive mark enrichment from the inactive X, and dysregulation of autosomal gene expression (Fig. 8A,B). In the future, mechanisms underlying these phenotypic outcomes need to be explored.

Methods

Cell culture

XEN cells used for this study are hybrid and carry maternal active X (X^{Mol}) and paternal inactive X (X^{Mus}) as reported previously (Cloutier et al. 2018; Arava et al. 2023; Naik et al. 2024). XEN cells were cultured in Dulbecco's Modified Eagle Medium (DMEM) (Himedia, #AL007A) as described previously (Naik et al. 2024). Media was supplemented with 20% fetal bovine serum (GIBCO, #10270-106), 3 mM L-glutamine (GIBCO, #25030081), 1.5× MEM nonessential amino acids (GIBCO, #1140-050), Pen-Strep (GIBCO, #15140122), and β-mercaptoethanol (Sigma-Aldrich, #M3148). Cells were grown on gelatin (Himedia, # TCL059)-coated plates at 37°C with 5% CO_2 and passaged using 0.05% trypsin.

CRISPR-based knockout cell line generation

Different *Xist* upstream deletion clones (D1, D2, and D3) were generated through CRISPR-Cas9-based approaches using pairs of small

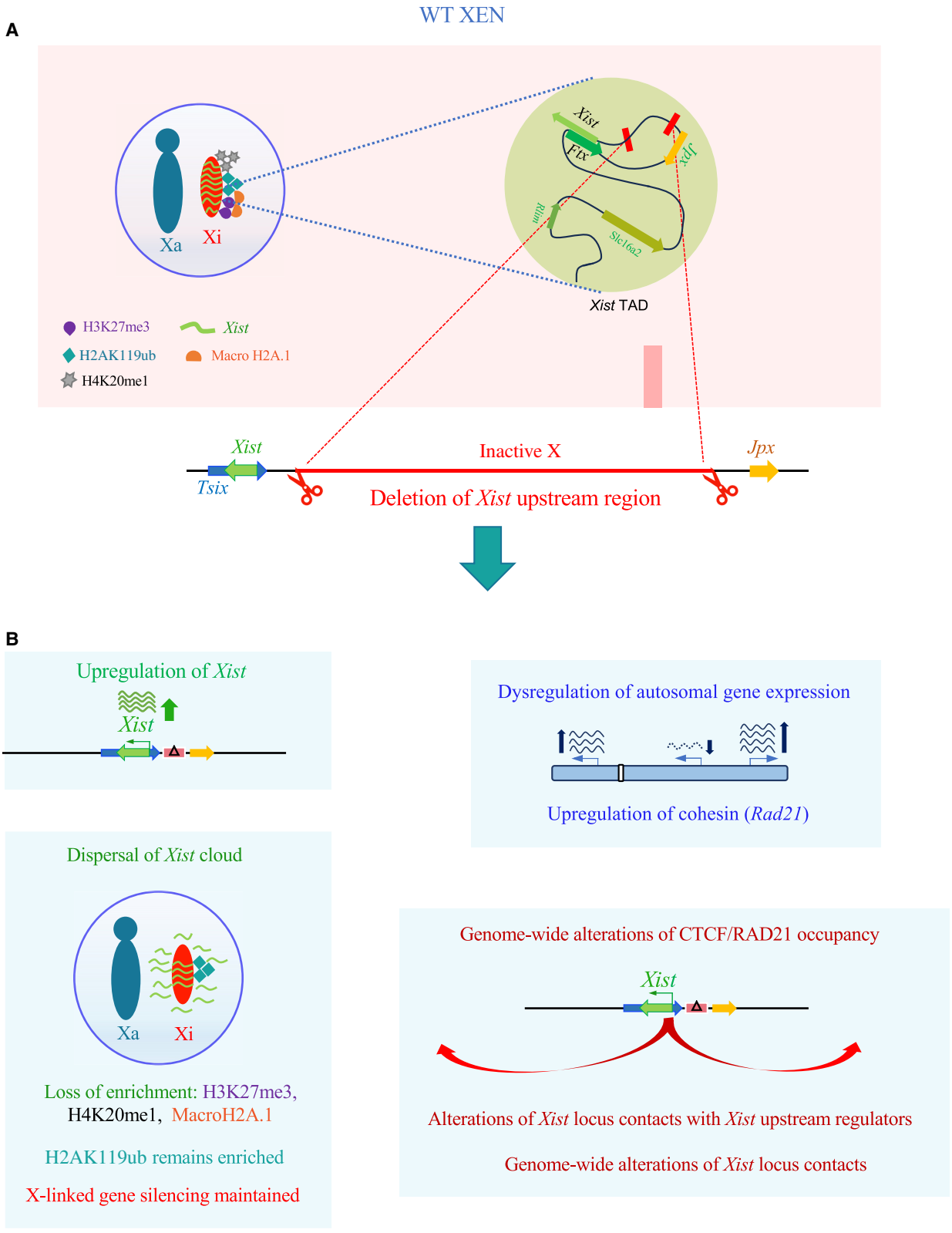

Figure 8. Deletion of *Xist* upstream sequence leads to diverse outcomes. (*A*) Model representing inactive X in XEN cells coated with *Xist* along with different repressive chromatin marks: H3K27me3, H2AK119ub, H4K20me1, and MacroH2A.1. *Right* side schematic showing the topological contacts of *Xist* with its upstream regulator. (*B*) Model showing that *Xist* upstream deletion on the inactive X leads to diverse outcomes such as (1) upregulation of *Xist*, (2) dispersal of *Xist* coating, loss of enrichment of repressive chromatin marks: H3K27me3, H4K20me1, and MacroH2A.1, (3) dysregulation of autosomal gene expression including upregulation of cohesin (*Rad21*), (4) genome-wide alterations of CTCF/RAD21 occupancy, (5) alterations of *Xist* locus contacts with *Xist* upstream regulators, and (6) genome-wide alterations of *Xist* locus contacts.

guide RNAs (sgRNAs) targeting specific genomic regions, designed using an online tool CHOPCHOP (https://chopchop.cbu.uib.no) and checked against off-target effects using the tool Cas-offinder (http://www.rgenome.net/cas-offinder/). sgRNAs used for different deletion clones are as follows: (1) For D1- sgRNA1: CAAGATTACTATTTTACCCCAGG; sgRNA2: GACCAAGGCGGGGTAGAAGAAGG. (2) For D2- sgRNA1: CAAGATTACTATTTTACCCCAGG; sgRNA2: AATTATAGGAGGGCTTCACATGG. (3) For D3- sgRNA1: AATTATAGGAGGGCTTCACATGG; sgRNA2: GACCAAGGCGGGGTAGAAGAAGG.

In brief, sgRNAs were cloned individually into the plasmid pSpCas9(BB)-2A-Puro (PX459) V2.0 (Addgene, #62988) and then transfected into XEN cells using Xfect transfection reagent (Clontech, #631318) in the presence of 1× Opti-MEM (GIBCO, #31985-070). Next, after selection through Puromycin (3 ug/mL), clones were FACS-sorted in 96-well plates as single cells and expanded for PCR screening, followed by Sanger sequencing. The nature of the heterozygous clones (carrying paternal or maternal deletion) was differentiated through PCR conducted using primers spanning single-nucleotide polymorphisms. All primers used for the screening are listed in Supplemental Table S5.

RNA FISH

For RNA FISH, we generated double-stranded RNA-FISH (dsRNA FISH) probes through random priming of BAC templates (*Xist, Atrx, Rlim, Pgk1*) using the Bioprime labeling kit (Invitrogen, #18094-011). Probes were labeled using Cy3-dUTP (Enzo Life Sciences, #ENZ-42501) and purified through ProbeQuant G-50 Micro columns (Cytiva, #28903408). Strand-specific RNA-FISH (ssRNA FISH) probes were produced using the MAXIscript T3/T7 kit (Ambion, #AM1326). ssRNA FISH probes were labeled using FITC-UTP and purified through Mini Quick Spin RNA columns (Roche, #11814427001). Labeled double-stranded and ssRNA FISH probes were then precipitated in the presence of 0.3 M sodium acetate (Sigma-Aldrich, #71196) and 0.5 M ammonium acetate (Sigma-Aldrich, #09691), respectively, along with 300 µg of yeast tRNA (Invitrogen, #15401011), 150 µg of sheared salmon sperm DNA (Invitrogen, #15632-011), and absolute ethanol (Hayman, #F205220) at 13,000 rpm for 20 mins at 4°C. The pellet was washed with 70% and then 100% ethanol, vacuum-dried and resuspended in deionized formamide (VWR Life Sciences, #0606) and then denatured at 95°C for 10 min followed by immediate snap-freezing on ice. A hybridization solution containing 20% dextran sulphate (SRL, #76203) and 2× SSC (SRL, #12590) was mixed with the denatured solution, and the probes were then stored at −20°C until use.

For RNA-FISH, cells were permeabilized and fixed as described below. Cells mounted on coverslips or on which IF had been conducted (fixed after IF with 2% PFA) were first dehydrated through an ethanol series of 70%, 85%, 95%, and 100% for 2 min each and air-dried. Cells were then hybridized with double-stranded or single-stranded probes overnight at 37°C. On the next day, cells were washed thrice with 2× SSC/50% formamide and 2× SSC, and twice with 1× SSC for 7 min each at 37°C. DAPI (Invitrogen, #D1306) diluted to 1:1000 was added at the third 2× SSC wash. The coverslips were finally mounted using Vectashield (Vector Labs, #H1000) and sealed with nail polish before visualization and image acquisition.

Immunofluorescence followed by RNA-FISH

For immunofluorescence, XEN cells were grown on gelatin (Himedia, #TCL059)-coated coverslips, followed by their permeabilization with ice-cold Cytoskeletal (CSK) buffer (composed of 300 mM Sucrose, 100 mM NaCl, 3 mM $MgCl_2$, and 10 mM PIPES buffer, pH 6.8) for 30 sec, followed by treatment with CSK buffer containing 0.4% Triton X-100 for 30 sec and another round of CSK buffer for 30 sec. Cells were then fixed using 3% paraformaldehyde (Electron Microscopy Sciences, #15710) for 10 min, washed 3× with 70% ethanol, and then stored at −20°C in 70% ethanol before conducting IF or RNA-FISH. For IF, XEN cells plated on 22-µm coverslips (Blue Star) were washed 3× with PBS (Himedia, #TL1006) for 3 min while shaking, following which they were incubated in blocking buffer composed of 0.5 mg/mL BSA (New England Biolabs, #B9001S), 80 units of RNAse-OUT RNAse inhibitor (Invitrogen, #10777-019), 0.2% Tween-20 (Promega, #H5152), and PBS for 30 min in a chamber humidified using PBS/0.2% Tween-20 at 37°C. Cell samples were then incubated with appropriately diluted primary antibody for 1 h at 37°C. The anti-trimethyl Histone H3 (Lys27) antibody (Merck, #07-449) was used at a dilution of 1:2500, the anti-Ubiquityl-Histone H2A (Lys119) antibody (CST, #8240T) at a dilution of 1:1600, the H4K20me1 antibody (ABclonal, # A2370) at a dilution of 1:80, the MacroH2A.1 antibody (ABclonal, #A9059) at a dilution of 1:400, the CIZ1 antibody (ABclonal, #A17349) at a dilution of 1:500, the CELF1 antibody (Invitrogen, #MA1-16675) at a dilution of 1:80, and the FBL antibody (ABclonal, #A1136) at a dilution of 1:200. Samples were then washed using PBS/0.2% Tween-20 3× for 3 min each, while shaking at 37°C, following which they were incubated with 1:300 diluted fluorescently conjugated secondary antibody (Alexa Fluor, Invitrogen, #A21428 and #A21422). Cell samples were then washed 3× with PBS/0.2% Tween-20 for 3 min each at 37°C and processed further for RNA-FISH as described above.

RT-qPCR

For RT-qPCR, RNA was isolated from XEN cells following the TRIzol (Ambion) method. RNA was first reverse-transcribed using the Primescript 1st strand cDNA synthesis kit (TaKaRa, #6110A) with random hexamers at 30°C for 10 min, 42°C for 60 min, followed by heat inactivation of the reverse transcriptase enzyme at 95°C for 5 min. Real time PCR was performed on the cDNA using the KAPA SYBR FAST qPCR master mix (2×) kit (Roche, #KK4618) with intron spanning primers in a QuantStudio 3 Real-time PCR system. All Ct values were normalized against *Tbp*. A 2^-ΔΔCt method was followed to calculate all relative fold changes of the genes. All RT-qPCR primers used for this study have been listed in Supplemental Table S5.

RNA sequencing and analysis

RNA sequencing and analysis was performed as described previously with few modifications (Naik et al. 2024). In brief, total RNA was isolated from XEN cells using TRIzol (Life Technologies, #15596-026) following the manufacturer's protocol. Next, quality of the RNA was checked through Bioanalyzer and used for the library preparation. The RNA-seq library was prepared following the manufacturer's protocol using the NEBNext/TruSeq library preparation kit and sequenced on the Illumina platform using pair-end (2 × 150 bp) chemistry. For data analysis, first FastQC of the transcriptomic sequencing reads was performed and adapter content were removed using Trim Galore! (v0.6.6) (http://www.bioinformatics.babraham.ac.uk/projects/trim_galore/). Further, the rRNA reads were removed using RiboDetector (v0.2.7) (Deng et al. 2022). Next, the STAR (2.7.9a) tool was used to map the transcriptomic sequencing reads to the mouse genome GRCm38 (mm10) (Dobin et al. 2013). Counting of reads was done using featureCounts (2.0.1) (Liao et al. 2014). For differential

gene expression analysis, R package DESeq2 tool was used (Love et al. 2014). The potential batch effect was accounted prior to differential gene expression analysis by correcting gene counts using ComBat-seq, where it was required (Zhang et al. 2020). For Gene Ontology to identify enriched biological processes, we used gprofiler g:GOSt (https://biit.cs.ut.ee/gprofiler/gost).

Allele-specific RNA-seq analysis

Allele-specific analysis of RNA-seq data was performed following the previously described method (Naik et al. 2021, 2022, 2024). In brief, an in silico reference genome was constructed by incorporating available strain-specific SNPs (https://www.sanger.ac.uk/science/data/mouse-genomes-project) into the mm10 reference genome using VCFtools. Next, transcriptomic reads were mapped separately to in silico-created parental genomes using STAR. To profile allelic read counts, an average of SNP-wise reads for a gene was calculated. Only those SNPs were considered that had a minimum read count of 10 per SNP site. Next, genes were filtered if they had at least two informative SNPs. Finally, the allelic ratio was calculated using the following formula: (Allele-Mus or Allele-Mol/Allele-Mus + Allele-Mol).

ChIP sequencing

For chromatin immunoprecipitation (ChIP), we used the Simple ChIP Enzymatic Chromatin IP kit with magnetic beads (Cell Signalling Technology, #9003) and followed the manufacturer's instructions with some modifications. In brief, cells were fixed with 1% formaldehyde (Sigma-Aldrich, #F8775) in DMEM (Himedia, #AL007A) by incubating at room temperature for 20 min, and then quenching was performed with 125 mM glycine by incubating for 5 min at room temperature. Following this, cells were washed with ice-cold phosphate-buffered saline (PBS) and then harvested for lysis. Cells were lysed using the lysis buffer provided in the kit by keeping them on ice. Following the lysis step, the nuclei were isolated. Chromatin was fragmented by digestion with micrococcal nuclease (provided in the kit), followed by sonication with Bioruptor pico (Diagenode) for 20 cycles, 30 sec on/off. Next, the chromatin was immunoprecipitated using ~1–5 µg of different antibodies. The sources of ChIP antibodies are provided in Supplemental Table S5. Isotype control IgG was used from the Simple ChIP Enzymatic Chromatin IP kit with magnetic beads (Cell Signalling Technology, #9003). Two percent of input chromatin DNA was kept aside before IP. The immunoprecipitated chromatin and input chromatin were reverse-cross-linked, purified, and quantified using Qubit (Thermo Fisher Scientific). After initial quality control, ChIP DNA was subjected to library preparation, and libraries were sequenced on the Illumina HiSeq platform using 150 × 2 paired-end chemistry.

ChIP-seq and CUT&RUN analyses

First, we performed peak calling before separating the allelic reads for our ChIP-seq and CUT&RUN analysis. Quality controlled reads were mapped against GRCm38 (mm10) using Bowtie 2 (Langmead and Salzberg 2012), and blacklisted regions were removed according to the ENCODE Project Consortium using BEDTools (v2.30.0) (Quinlan and Hall 2010). The MACS2 (v2.2.7.1) tool was used for peak calling with parameters -f BAMPE -g 2652783500 --keep-dup all --nomodel (Zhang et al. 2008). To identify significant peaks, we used different significant *Q*-values: for ChIP-seq; CTCF <0.00001, RAD21 <0.01, and histone—H3K27ac <0.00001; H3K9me3, H3K27me3, and H3K4me1 <0.05, and for CUT&RUN <0.05. CTCF motif was identified using FIMO tool based on the JASPAR (MA0139.1) database using a *P*-value cutoff of 0.001 (Grant et al. 2011).

Allele-specific ChIP-seq analysis was performed following the methods as described previously (Ayyamperumal et al. 2024). In short, a GRCm38 (mm10) N-masked in silico genome was created using SNPsplit genome preparation. Next, ChIP-seq reads were mapped to the in silico-created N-masked genome using Bowtie 2 (Langmead and Salzberg 2012). Blacklisted regions were removed from our analysis according to the ENCODE Project Consortium. SNPsplit (0.4.0) was then used to create allele-specific BAM files by segregating the aligned reads into two distinct alleles (Krueger and Andrews 2016). Next, BPM-normalized bigWig files were generated using the bamCoverage function from deepTools (v.3.5.0) (Ramírez et al. 2016). Next, we calculated the allelic ratio for each corresponding individual peak, identified through nonallelic peak calling as described above. We calculated the allelic ratio using the following formula: (Allele-A or Allele-B/Allele-A + Allele-B). Peaks with allelic ratio >0.80 were considered as monoallelic and the rest were assigned as biallelic peaks. Enrichment plots were generated using function ComputeMatrix followed by plotHeatmap using deepTools (Ramírez et al. 2016). The previously published ChIP-seq and CUT&RUN data set used for this study is available at the NCBI Gene Expression Omnibus (GEO; https://www.ncbi.nlm.nih.gov/geo/) (Supplemental Table S1).

Circular chromosome conformation capture (4C) sequencing and analysis

XEN cells (~10 million) were grown under appropriate conditions and fixed using 1.5% formaldehyde (Sigma-Aldrich, #F8775) while shaking at 40 rpm. Formaldehyde was quenched using 125 mM glycine (Cell Signalling Technology, #7005). Cells were washed with ice-cold PBS (2×), scraped, and pelleted before storing them at −80°C. Cells were lysed using Tris-Cl pH 8.0 (10 mM), NaCl (10 mM), NP-40 (0.2%), and PIC (1×), homogenized by a dounce homogenizer (15 strokes with each of pestle A and pestle B) and pelleted down. The nuclei pellet was then washed 2× with ice-cold 1× DPBS and resuspended in restriction digestion buffer. The pellet was then incubated at 65°C in the presence of 1% SDS to get rid of uncrosslinked proteins for 8 min and then immediately transferred to ice. The SDS was neutralized using 10% TritonX-100, following which the chromatin was digested using 100 units of the 1st cutter NlaIII (NEB, #R0125L) overnight at 37°C. The digested chromatin was then subjected to ligation using T4 DNA ligase (Invitrogen) and T4 DNA Ligase buffer (NEB, #B0202S) at 16°C for 4 h. The ligated samples were decrosslinked overnight using Proteinase K (Roche, #3115887001), PCR-purified, and ethanol-precipitated. Fifty units of DpnII (NEB, #R0543M) were used for the second restriction digestion, following which samples were again ligated, purified, and precipitated similarly to obtain the 4C library. The 4C library was treated with RNase A and purified using the QIAquick PCR purification kit. The concentration of the 4C library was quantified, and PCR was conducted using specific viewpoint oligos. The oligo sequences used for 4C are summarized in Supplemental Table S5. The amplified product was then PCR-purified and subjected to high-throughput sequencing using HiSeq 2500. Data were analyzed using the R tool pipe4c (v1.16) (https://github.com/deLaatLab/pipe4C) pipeline with default parameters (Krijger et al. 2020). In brief, reads were demultiplexed and mapped using Bowtie 2 against mm10. To achieve allelic resolution of viewpoint interaction, reads were split based on SNP present on read2. r3Cseq v(1.50.0) from R was used to identify significant interactions (*Q*-value <0.01) (Thongjuea et al. 2013). RPM-normalized bigWig files were used to visualize the 4C interaction. Virtual 4C analysis using HiC data was performed

using cooltools (Abdennur et al. 2024). The previously published HiC data set used for this study is available at GEO (Supplemental Table S1).

Data visualization and plots

All plots were generated using R version 4.2.1 using ggplot2 (Wickham et al. 2016), and Python package pyGenomeTracks was used to generate genomic tracks (Lopez-Delisle et al. 2021).

Microscopy

RNA-FISH and IF images were captured using Olympus IX73 Research Inverted microscope and cellSens [Ver.2.1] Life Science imaging software equipped with a 100× oil-immersion objective. Z-stacks for each image were acquired at a 0.25-μm step size, and EFI processing was conducted to get the maximum intensity projection of the image. For area and sphericity measurements, *Xist* clouds were defined in the wild-type and mutant cells using the ROI (region of interest) option, and the measurements were derived from the measurements and ROI tool of the cellSens imaging software. Intensity profile of H3K27me3 across the *Xist* cloud was measured using the line Profile tool window, and measurements were exported as a chart for plotting the profile. *Xist*-nucleolar association measurements were performed based on single z-sections.

Data access

All raw and processed sequencing data (RNA-seq, ChIP-seq, and 4C-seq) generated in this study have been submitted to the NCBI Gene Expression Omnibus (GEO; https://www.ncbi.nlm.nih.gov/geo/) under accession number GSE245643.

Competing interest statement

The authors declare no competing interests.

Acknowledgments

We thank Prof. Sundeep Kalantry, University of Michigan for providing BACs and cell line. We thank NCBS genomic core facility for the sequencing. We acknowledge the support from the high-performance computing facility "Beagle" at the Indian Institute of Science (IISc) under the Department of Biotechnology (DBT), Government of India-IISc partnership program. This study is supported by DBT (BT/PR30399/BRB/10/1746/2018), DST-SERB (CRG/2019/003067), Anusandhan National Research Foundation (ANRF) (CRG/2022/008605), DBT-Ramalingaswamy fellowship (BT/RLF/Re-entry/05/2016), and Infosys Young Investigator grant award to S.G. S.M., A.M., and A.J.N. acknowledge University Grants Commission (UGC) for the fellowship. R.B. acknowledges the Council of Scientific and Industrial Research (CSIR), India for the fellowship. L.S.B. acknowledges the DST Women Scientist Award.

Author contributions: S.G. supervised and acquired the funding for the study. S.G. and S.M. conceptualized the study. S.M., L.S.B., R.B., A.M., A.K., A.J.N., and G.S.B. performed experiments. H.C.N. performed all bioinformatic analysis. D.N. supervised and helped with the 4C experiments, and S.N. helped with the 4C analysis. S.M. wrote the first draft of the manuscript. H.C.N. and L.S.B. contributed to writing the manuscript. S.G. and S.M. edited and proofread the manuscript. The final manuscript was approved by all the authors.

References

Abdennur N, Abraham S, Fudenberg G, Flyamer IM, Galitsyna AA, Goloborodko A, Imakaev M, Oksuz BA, Venev SV, Xiao Y. 2024. Cooltools: enabling high-resolution Hi-C analysis in Python. *PLoS Comput Biol* **20:** e1012067. doi:10.1371/journal.pcbi.1012067

Arava M, Majumdar S, Bammidi LS, Naik HC, Baro R, Gayen S. 2023. Gene-specific reactivation of X-linked genes upon Xist loss is linked to the chromatin states in extraembryonic endoderm and epiblast stem cells. bioRxiv doi:10.1101/2023.10.20.563299

Ayyamperumal P, Naik HC, Naskar AJ, Bammidi LS, Gayen S. 2024. Epigenomic states contribute to coordinated allelic transcriptional bursting in iPSC reprogramming. *Life Sci Alliance* **7:** e202302337. doi:10.26508/lsa.202302337

Barakat TS, Loos F, Van Staveren S, Myronova E, Ghazvini M, Grootegoed JA, Gribnau J. 2014. The *trans*-activator RNF12 and *cis*-acting elements effectuate X chromosome inactivation independent of X-pairing. *Mol Cell* **53:** 965–978. doi:10.1016/j.molcel.2014.02.006

Barutcu AR, Maass PG, Lewandowski JP, Weiner CL, Rinn JL. 2018. A TAD boundary is preserved upon deletion of the CTCF-rich *Firre* locus. *Nat Commun* **9:** 1444. doi:10.1038/s41467-018-03614-0

Boeren J, Gribnau J. 2021. Xist-mediated chromatin changes that establish silencing of an entire X chromosome in mammals. *Curr Opin Cell Biol* **70:** 44–50. doi:10.1016/j.ceb.2020.11.004

Calabrese JM, Sun W, Song L, Mugford JW, Williams L, Yee D, Starmer J, Mieczkowski P, Crawford GE, Magnuson T. 2012. Site-specific silencing of regulatory elements as a mechanism of X inactivation. *Cell* **151:** 951–963. doi:10.1016/j.cell.2012.10.037

Chaumeil J, Le Baccon P, Wutz A, Heard E. 2006. A novel role for Xist RNA in the formation of a repressive nuclear compartment into which genes are recruited when silenced. *Genes Dev* **20:** 2223–2237. doi:10.1101/gad.380906

Chen CK, Blanco M, Jackson C, Aznauryan E, Ollikainen N, Surka C, Chow A, Cerase A, McDonel P, Guttman M. 2016. Xist recruits the X chromosome to the nuclear lamina to enable chromosome-wide silencing. *Science (1979)* **354:** 468–472. doi:10.1126/science.aae0047

Chow JC, Ciaudo C, Fazzari MJ, Mise N, Servant N, Glass JL, Attreed M, Avner P, Wutz A, Barillot E, et al. 2010. LINE-1 activity in facultative heterochromatin formation during X chromosome inactivation. *Cell* **141:** 956–969. doi:10.1016/j.cell.2010.04.042

Chureau C, Chantalat S, Romito A, Galvani A, Duret L, Avner P, Rougeulle C. 2011. Ftx is a non-coding RNA which affects Xist expression and chromatin structure within the X-inactivation center region. *Hum Mol Genet* **20:** 705–718. doi:10.1093/hmg/ddq516

Cifuentes-Rojas C, Hernandez AJ, Sarma K, Lee JT. 2014. Regulatory interactions between RNA and polycomb repressive complex 2. *Mol Cell* **55:** 171–185. doi:10.1016/j.molcel.2014.05.009

Clerc P, Avner P. 2003. Multiple elements within the Xic regulate random X inactivation in mice. *Semin Cell Dev Biol* **14:** 85–92. doi:10.1016/S1084-9521(02)00140-4

Cloutier M, Harris C, Gayen S, Maclary E, Kalantry S. 2018. Experimental analysis of imprinted mouse X-chromosome inactivation. *Methods Mol Biol* **1861:** 177–203. doi:10.1007/978-1-4939-8766-5_14

Collombet S, Ranisavljevic N, Nagano T, Varnai C, Shisode T, Leung W, Piolot T, Galupa R, Borensztein M, Servant N, et al. 2020. Parental-to-embryo switch of chromosome organization in early embryogenesis. *Nature* **580:** 142–146. doi:10.1038/s41586-020-2125-z

Darrow EM, Huntley MH, Dudchenko O, Stamenova EK, Durand NC, Sun Z, Huang SC, Sanborn AL, Machol I, Shamim M, et al. 2016. Deletion of *DXZ4* on the human inactive X chromosome alters higher-order genome architecture. *Proc Natl Acad Sci* **113:** E4504–E4512. doi:10.1073/pnas.1609643113

Davidovich C, Cech TR. 2015. The recruitment of chromatin modifiers by long noncoding RNAs: lessons from PRC2. *RNA* **21:** 2007–2022. doi:10.1261/rna.053918.115

Deng X, Ma W, Ramani V, Hill A, Yang F, Ay F, Berletch JB, Blau CA, Shendure J, Duan Z, et al. 2015. Bipartite structure of the inactive mouse X chromosome. *Genome Biol* **16:** 152. doi:10.1186/s13059-015-0728-8

Deng ZL, Münch PC, Mreches R, McHardy AC. 2022. Rapid and accurate identification of ribosomal RNA sequences via deep learning. *Nucleic Acids Res* **50:** e60. doi:10.1093/nar/gkac112

Despang A, Schöpflin R, Franke M, Ali S, Jerković I, Paliou C, Chan WL, Timmermann B, Wittler L, Vingron M, et al. 2019. Functional dissection of the Sox9–Kcnj2 locus identifies nonessential and instructive roles of TAD architecture. *Nat Genet* **51:** 1263–1271. doi:10.1038/s41588-019-0466-z

Dobin A, Davis CA, Schlesinger F, Drenkow J, Zaleski C, Jha S, Batut P, Chaisson M, Gingeras TR. 2013. STAR: ultrafast universal RNA-seq aligner. *Bioinformatics* **29:** 15–21. doi:10.1093/bioinformatics/bts635

Dror I, Chitiashvili T, Tan SYX, Cano CT, Sahakyan A, Markaki Y, Chronis C, Collier AJ, Deng W, Liang G, et al. 2024. XIST directly regulates X-linked

and autosomal genes in naive human pluripotent cells. *Cell* **187:** 110–129.e31. doi:10.1016/j.cell.2023.11.033
Du Z, Hu L, Zou Z, Liu M, Li Z, Lu X, Harris C, Xiang Y, Chen F, Yu G, et al. 2024. Stepwise de novo establishment of inactive X chromosome architecture in early development. *Nat Genet* **56:** 2185–2198. doi:10.1038/s41588-024-01897-2
Fang H, Bonora G, Lewandowski JP, Thakur J, Filippova GN, Henikoff S, Shendure J, Duan Z, Rinn JL, Deng X, et al. 2020. *Trans*- and *cis*-acting effects of *Firre* on epigenetic features of the inactive X chromosome. *Nat Commun* **11:** 6053. doi:10.1038/s41467-020-19879-3
Froberg JE, Pinter SF, Kriz AJ, Jégu T, Lee JT. 2018. Megadomains and superloops form dynamically but are dispensable for X-chromosome inactivation and gene escape. *Nat Commun* **9:** 5004. doi:10.1038/s41467-018-07446-w
Furlan G, Gutierrez Hernandez N, Huret C, Galupa R, van Bemmel JG, Romito A, Heard E, Morey C, Rougeulle C. 2018. The *Ftx* noncoding locus controls X chromosome inactivation independently of its RNA products. *Mol Cell* **70:** 462–472.e8. doi:10.1016/j.molcel.2018.03.024
Galupa R. 2023. Lppnx lncRNA: the new kid on the block or an old friend in X-inactivation choice? *Proc Natl Acad Sci* **120:** e2218989120. doi:10.1073/pnas.2218989120
Galupa R, Heard E. 2018. X-chromosome inactivation: a crossroads between chromosome architecture and gene regulation. *Annu Rev Genet* **52:** 535–566. doi:10.1146/annurev-genet-120116-024611
Galupa R, Nora EP, Worsley-Hunt R, Picard C, Gard C, van Bemmel JG, Servant N, Zhan Y, El Marjou F, Johanneau C, et al. 2020. A conserved noncoding locus regulates random monoallelic Xist expression across a topological boundary. *Mol Cell* **77:** 352–367.e8. doi:10.1016/j.molcel.2019.10.030
Galupa R, Picard C, Servant N, Nora EP, Zhan Y, van Bemmel JG, El Marjou F, Johanneau C, Borensztein M, Ancelin K, et al. 2022. Inversion of a topological domain leads to restricted changes in its gene expression and affects interdomain communication. *Development* **149:** dev200568. doi:10.1242/dev.200568
Gayen S, Maclary E, Buttigieg E, Hinten M, Kalantry S. 2015. A primary role for the Tsix lncRNA in maintaining random X-chromosome inactivation. *Cell Rep* **11:** 1251–1265. doi:10.1016/j.celrep.2015.04.039
Gayen S, Maclary E, Hinten M, Kalantry S. 2016. Sex-specific silencing of X-linked genes by Xist RNA. *Proc Natl Acad Sci* **113:** E309–E318. doi:10.1073/pnas.1515971113
Giorgetti L, Lajoie BR, Carter AC, Attia M, Zhan Y, Xu J, Chen CJ, Kaplan N, Chang HY, Heard E, et al. 2016. Structural organization of the inactive X chromosome in the mouse. *Nature* **535:** 575–579. doi:10.1038/nature18589
Gjaltema RAF, Schwämmle T, Kautz P, Robson M, Schöpflin R, Ravid Lustig L, Brandenburg L, Dunkel I, Vechiatto C, Ntini E, et al. 2022. Distal and proximal *cis*-regulatory elements sense X chromosome dosage and developmental state at the *Xist* locus. *Mol Cell* **82:** 190–208.e17. doi:10.1016/j.molcel.2021.11.023
Grant CE, Bailey TL, Noble WS. 2011. FIMO: scanning for occurrences of a given motif. *Bioinformatics* **27:** 1017–1018. doi:10.1093/bioinformatics/btr064
Harris C, Cloutier M, Trotter M, Hinten M, Gayen S, Du Z, Xie W, Kalantry S. 2019. Conversion of random x-inactivation to imprinted x-inactivation by maternal prc2. *eLife* **8:** e4425. doi:10.7554/eLife.44258
Hosoi Y, Soma M, Shiura H, Sado T, Hasuwa H, Abe K, Kohda T, Ishino F, Kobayashi S. 2018. Female mice lacking Ftx lncRNA exhibit impaired X-chromosome inactivation and a microphthalmia-like phenotype. *Nat Commun* **9:** 4618. doi:10.1038/s41467-018-07100-5
Jachowicz JW, Strehle M, Banerjee AK, Blanco MR, Thai J, Guttman M. 2022. Xist spatially amplifies SHARP/SPEN recruitment to balance chromosome-wide silencing and specificity to the X chromosome. *Nat Struct Mol Biol* **29:** 239–249. doi:10.1038/s41594-022-00739-1
Johnston CM, Nesterova TB, Formstone EJ, Newall AET, Duthie SM, Sheardown SA, Brockdorff N. 1998. Developmentally regulated Xist promoter switch mediates initiation of X inactivation. *Cell* **94:** 809–817. doi:10.1016/S0092-8674(00)81739-0
Jonkers I, Barakat TS, Achame EM, Monkhorst K, Kenter A, Rentmeester E, Grosveld F, Grootegoed JA, Gribnau J. 2009. RNF12 is an X-encoded dose-dependent activator of X chromosome inactivation. *Cell* **139:** 999–1011. doi:10.1016/j.cell.2009.10.034
Kelsey AD, Yang C, Leung D, Minks J, Dixon-McDougall T, Baldry SEL, Bogutz AB, Lefebvre L, Brown CJ. 2015. Impact of flanking chromosomal sequences on localization and silencing by the human non-coding RNA XIST. *Genome Biol* **16:** 208. doi:10.1186/s13059-015-0774-2
Krijger PHL, Geeven G, Bianchi V, Hilvering CRE, de Laat W. 2020. 4C-seq from beginning to end: a detailed protocol for sample preparation and data analysis. *Methods* **170:** 17–32. doi:10.1016/j.ymeth.2019.07.014
Krueger F, Andrews SR. 2016. SNPsplit: allele-specific splitting of alignments between genomes with known SNP genotypes. *F1000Res* **5:** 1479. doi:10.12688/f1000research.9037.1
Langmead B, Salzberg SL. 2012. Fast gapped-read alignment with Bowtie 2. *Nat Methods* **9:** 357–359. doi:10.1038/nmeth.1923
Lee JT, Davidow LS, Warshawsky D. 1999. *Tsix*, a gene antisense to *Xist* at the X-inactivation centre. *Nat Genet* **21:** 400–404. doi:10.1038/7734
Liao Y, Smyth GK, Shi W. 2014. featureCounts: an efficient general purpose program for assigning sequence reads to genomic features. *Bioinformatics* **30:** 923–930. doi:10.1093/bioinformatics/btt656
Loda A, Brandsma JH, Vassilev I, Servant N, Loos F, Amirnasr A, Splinter E, Barillot E, Poot RA, Heard E, et al. 2017. Genetic and epigenetic features direct differential efficiency of Xist-mediated silencing at X-chromosomal and autosomal locations. *Nat Commun* **8:** 690. doi:10.1038/s41467-017-00528-1
Lopez-Delisle L, Rabbani L, Wolff J, Bhardwaj V, Backofen R, Grüning B, Ramírez F, Manke T. 2021. pyGenomeTracks: reproducible plots for multivariate genomic datasets. *Bioinformatics* **37:** 422–423. doi:10.1093/bioinformatics/btaa692
Love MI, Huber W, Anders S. 2014. Moderated estimation of fold change and dispersion for RNA-seq data with DESeq2. *Genome Biol* **15:** 550. doi:10.1186/s13059-014-0550-8
Lyon MF. 1961. Gene action in the X-chromosome of the mouse (*Mus musculus* L). *Nature* **190:** 372–373. doi:10.1038/190372a0
Lyon MF. 1998. X-Chromosome inactivation: a repeat hypothesis. *Cytogenet Genome Res* **80:** 133–137. doi:10.1159/000014969
Maclary E, Buttigieg E, Hinten M, Gayen S, Harris C, Sarkar MK, Purushothaman S, Kalantry S. 2014. Differentiation-dependent requirement of Tsix long non-coding RNA in imprinted X-chromosome inactivation. *Nat Commun* **5:** 4209. doi:10.1038/ncomms5209
Maclary E, Hinten M, Harris C, Sethuraman S, Gayen S, Kalantry S. 2017. PRC2 represses transcribed genes on the imprinted inactive X chromosome in mice. *Genome Biol* **18:** 82. doi:10.1186/s13059-017-1211-5
Mak W, Nesterova TB, De Napoles M, Appanah R, Yamanaka S, Otte AP, Brockdorff N. 2004. Reactivation of the paternal X chromosome in early mouse embryos. *Science (1979)* **303:** 666–669. doi:10.1126/science.1092674
Malcore RM, Kalantry S. 2024. A comparative analysis of mouse imprinted and random X-chromosome inactivation. *Epigenomes* **8:** 8. doi:10.3390/epigenomes8010008
Mandal S, Chandel D, Kaur H, Majumdar S, Arava M, Gayen S. 2020. Single-cell analysis reveals partial reactivation of X chromosome instead of chromosome-wide dampening in naive human pluripotent stem cells. *Stem Cell Reports* **14:** 745–754. doi:10.1016/j.stemcr.2020.03.027
Minajigi A, Froberg JE, Wei C, Sunwoo H, Kesner B, Colognori D, Lessing D, Payer B, Boukhali M, Haas W, et al. 2015. A comprehensive Xist interactome reveals cohesin repulsion and an RNA-directed chromosome conformation. *Science* **349:** aab2276. doi:10.1126/science.aab2276
Naik HC, Hari K, Chandel D, Mandal S, Jolly MK, Gayen S. 2021. Semicoordinated allelic-bursting shape dynamic random monoallelic expression in pregastrulation embryos. *iScience* **24:** 102954. doi:10.1016/j.isci.2021.102954
Naik HC, Hari K, Chandel D, Jolly MK, Gayen S. 2022. Single-cell analysis reveals X upregulation is not global in pre-gastrulation embryos. *iScience* **25:** 104465. doi:10.1016/j.isci.2022.104465
Naik HC, Chandel D, Majumdar S, Arava M, Baro R, Bv H, Hari K, Ayyamperumal P, Manhas A, Jolly MK, et al. 2024. Lineage-specific dynamics of loss of X upregulation during inactive-X reactivation. *Stem Cell Reports* **19:** 1564–1582. doi:10.1016/j.stemcr.2024.10.001
Newall AET, Duthie S, Formstone E, Nesterova T, Alexiou M, Johnston C, Caparros ML, Brockdorff N. 2001. Primary non-random X inactivation associated with disruption of Xist promoter regulation. *Hum Mol Genet* **10:** 581–589. doi:10.1093/hmg/10.6.581
Nora EP, Lajoie BR, Schulz EG, Giorgetti L, Okamoto I, Servant N, Piolot T, Van Berkum NL, Meisig J, Sedat J, et al. 2012. Spatial partitioning of the regulatory landscape of the X-inactivation centre. *Nature* **485:** 381–385. doi:10.1038/nature11049
Ogawa Y, Lee JT. 2003. *Xite*, X-inactivation intergenic transcription elements that regulate the probability of choice. *Mol Cell* **11:** 731–743. doi:10.1016/S1097-2765(03)00063-7
Okamoto I, Otte AP, Allis CD, Reinberg D, Heard E. 2004. Epigenetic dynamics of imprinted X inactivation during early mouse development. *Science* **303:** 644–649. doi:10.1126/science.1092727
Pandya-Jones A, Markaki Y, Serizay J, Chitiashvili T, Mancia Leon WR, Damianov A, Chronis C, Papp B, Chen CK, McKee R, et al. 2020. A protein assembly mediates *Xist* localization and gene silencing. *Nature* **587:** 145–151. doi:10.1038/s41586-020-2703-0
Poonperm R, Ichihara S, Miura H, Tanigawa A, Nagao K, Obuse C, Sado T, Hiratani I. 2023. Replication dynamics identifies the folding principles of the inactive X chromosome. *Nat Struct Mol Biol* **30:** 1224–1237. doi:10.1038/s41594-023-01052-1
Quinlan AR, Hall IM. 2010. BEDTools: a flexible suite of utilities for comparing genomic features. *Bioinformatics* **26:** 841–842. doi:10.1093/bioinformatics/btq033

Ramírez F, Ryan DP, Grüning B, Bhardwaj V, Kilpert F, Richter AS, Heyne S, Dündar F, Manke T. 2016. deepTools2: a next generation web server for deep-sequencing data analysis. *Nucleic Acids Res* **44:** W160–W165. doi:10.1093/nar/gkw257

Ravid Lustig L, Sampath Kumar A, Schwämmle T, Dunkel I, Noviello G, Limberg E, Weigert R, Pacini G, Buschow R, Ghauri A, et al. 2023. GATA transcription factors drive initial Xist upregulation after fertilization through direct activation of long-range enhancers. *Nat Cell Biol* **25:** 1704–1715. doi:10.1038/s41556-023-01266-x

Ridings-Figueroa R, Stewart ER, Nesterova TB, Coker H, Pintacuda G, Godwin J, Wilson R, Haslam A, Lilley F, Ruigrok R, et al. 2017. The nuclear matrix protein CIZ1 facilitates localization of Xist RNA to the inactive X-chromosome territory. *Genes Dev* **31:** 876–888. doi:10.1101/gad.295907.117

Romer JT, Ashworth A. 2000. The upstream region of the mouse *Xist* gene contains two ribosomal protein pseudogenes. *Mamm Genome* **11:** 461–463. doi:10.1007/s003350010087

Rosspopoff O, Cazottes E, Huret C, Loda A, Collier AJ, Casanova M, Rugg-Gunn PJ, Heard E, Ouimette JF, Rougeulle C. 2023. Species-specific regulation of *XIST* by the *JPX*/*FTX* orthologs. *Nucleic Acids Res* **51:** 2177–2194. doi:10.1093/nar/gkad029

Rougeulle C, Avner P. 1996. Identification of an *S19* pseudogene lying close to the *Xist* sequence in the mouse. *Mamm Genome* **7:** 606–607. doi:10.1007/s003359900179

Samanta MK, Gayen S, Harris C, Maclary E, Murata-Nakamura Y, Malcore RM, Porter RS, Garay PM, Vallianatos CN, Samollow PB, et al. 2022. Activation of *Xist* by an evolutionarily conserved function of KDM5C demethylase. *Nat Commun* **13:** 2602. doi:10.1038/s41467-022-30352-1

Sarkar MK, Gayen S, Kumar S, Maclary E, Buttigieg E, Hinten M, Kumari A, Harris C, Sado T, Kalantry S. 2015. An Xist-activating antisense RNA required for X-chromosome inactivation. *Nat Commun* **6:** 8564. doi:10.1038/ncomms9564

Sheardown SA, Newall AET, Norris DP, Rastan S, Brockdorff N. 1997. Regulatory elements in the minimal promoter region of the mouse *Xist* gene. *Gene* **203:** 159–168. doi:10.1016/S0378-1119(97)00507-6

Shin J, Bossenz M, Chung Y, Ma H, Byron M, Taniguchi-Ishigaki N, Zhu X, Jiao B, Hall LL, Green MR, et al. 2010. Maternal Rnf12/RLIM is required for imprinted X-chromosome inactivation in mice. *Nature* **467:** 977–981. doi:10.1038/nature09457

Shin J, Wallingford MC, Gallant J, Marcho C, Jiao B, Byron M, Bossenz M, Lawrence JB, Jones SN, Mager J, et al. 2014. RLIM is dispensable for X-chromosome inactivation in the mouse embryonic epiblast. *Nature* **511:** 86–89. doi:10.1038/nature13286

Soma M, Fujihara Y, Okabe M, Ishino F, Kobayashi S. 2014. *Ftx* is dispensable for imprinted X-chromosome inactivation in preimplantation mouse embryos. *Sci Rep* **4:** 5181. doi:10.1038/srep05181

Splinter E, de Wit E, Nora EP, Klous P, van de Werken HJG, Zhu Y, Kaaij LJT, van Ijcken W, Gribnau J, Heard E, et al. 2011. The inactive X chromosome adopts a unique three-dimensional conformation that is dependent on Xist RNA. *Genes Dev* **25:** 1371–1383. doi:10.1101/gad.633311

Sun Y, Xu X, Zhao W, Zhang Y, Chen K, Li Y, Wang X, Zhang M, Xue B, Yu W, et al. 2023. RAD21 is the core subunit of the cohesin complex involved in directing genome organization. *Genome Biol* **24:** 155. doi:10.1186/s13059-023-02982-1

Takagi N, Sasaki M. 1975. Preferential inactivation of the paternally derived X chromosome in the extraembryonic membranes of the mouse. *Nature* **256:** 640–642. doi:10.1038/256640a0

Thongjuea S, Stadhouders R, Grosveld FG, Soler E, Lenhard B. 2013. r3Cseq: an R/Bioconductor package for the discovery of long-range genomic interactions from chromosome conformation capture and next-generation sequencing data. *Nucleic Acids Res* **41:** e132. doi:10.1093/nar/gkt373

Tian D, Sun S, Lee JT. 2010. The long noncoding RNA, Jpx, is a molecular switch for X chromosome inactivation. *Cell* **143:** 390–403. doi:10.1016/j.cell.2010.09.049

Valledor M, Byron M, Dumas B, Carone DM, Hall LL, Lawrence JB. 2023. Early chromosome condensation by XIST builds A-repeat RNA density that facilitates gene silencing. *Cell Rep* **42:** 112686. doi:10.1016/j.celrep.2023.112686

van Bemmel JG, Galupa R, Gard C, Servant N, Picard C, Davies J, Szempruch AJ, Zhan Y, Żylicz JJ, Nora EP, et al. 2019. The bipartite TAD organization of the X-inactivation center ensures opposing developmental regulation of *Tsix* and *Xist*. *Nat Genet* **51:** 1024–1034. doi:10.1038/s41588-019-0412-0

Wang F, Shin JD, Shea JM, Yu J, Bošković A, Byron M, Zhu X, Shalek AK, Regev A, Lawrence JB, et al. 2016. Regulation of X-linked gene expression during early mouse development by *Rlim*. *eLife* **5:** e19127. doi:10.7554/eLife.19127

Warshawsky D, Stavropoulos N, Lee JT. 1999. Further examination of the *Xist* promoter-switch hypothesis in X inactivation: evidence against the existence and function of a P(0) promoter. *Proc Natl Acad Sci* **96:** 14424–14429. doi:10.1073/pnas.96.25.14424

Wickham H. 2016. *ggplot2: elegant graphics for data analysis*. Springer-Verlag, New York. https://ggplot2.tidyverse.org.

Yang F, Deng X, Ma W, Berletch JB, Rabaia N, Wei G, Moore JM, Filippova GN, Xu J, Liu Y, et al. 2015. The lncRNA *Firre* anchors the inactive X chromosome to the nucleolus by binding CTCF and maintains H3K27me3 methylation. *Genome Biol* **16:** 52. doi:10.1186/s13059-015-0618-0

Zhang LF, Huynh KD, Lee JT. 2007. Perinucleolar targeting of the inactive X during S phase: evidence for a role in the maintenance of silencing. *Cell* **129:** 693–706. doi:10.1016/j.cell.2007.03.036

Zhang Y, Liu T, Meyer CA, Eeckhoute J, Johnson DS, Bernstein BE, Nusbaum C, Myers RM, Brown M, Li W, et al. 2008. Model-based Analysis of ChIP-Seq (MACS). *Genome Biol* **9:** R137. doi:10.1186/gb-2008-9-9-r137

Zhang Y, Parmigiani G, Johnson WE. 2020. ComBat-seq: batch effect adjustment for RNA-seq count data. *NAR Genom Bioinform* **2:** lqaa078. doi:10.1093/nargab/lqaa078

Żylicz JJ, Heard E. 2020. Molecular mechanisms of facultative heterochromatin formation: an X-chromosome perspective. *Annu Rev Biochem* **89:** 255–282. doi:10.1146/annurev-biochem-062917-012655

Received July 16, 2024; accepted in revised form July 8, 2025.